Chapter 3

III-V semiconductor on Si substrate

3.1   Introduction

The heteroepitaxy of III-V semiconductors on Si has the potential to enable integration of Si electronic circuits with III-V compound-based devices such as light emission and high speed operation into highly integrated Si-based electronic devices.   Among many III-V compounds, GaAs-based semiconductors on Si substrate (GaAs/Si) have attracted much interest as promising materials for future optoelectronic integrated circuits (OEICs).[1-8] In the conventional Si-based ultra large scale integrated circuit (ULSI) chip with GaAs-based optical input/output (I/O) devices can hopefully promise the increased I/O speed and increased resistance to electromagnetic interference without time delays by optical chip-to-chip interconnects and communications. The communications can be carried out by high-speed optical links coupled through fibers or free-space propagation.

However, GaAs/Si materials growth by heteroepitaxy suffers from three major problems:

1. the anti-phase domain (APD) generation due to the polar (GaAs)-on-nonpolar (Si) system;

2. the generation of high density of threading dislocations ($> 10^6$ cm^{-2}) due to the ~ 4 % mismatch between the lattice constants of GaAs (0.5653 nm) and Si (0.5431 nm); and

3. the large biaxial tensile stress ($\sim 10^9$ dyn/cm^2) generated during cooling after the growth due to the difference in the thermal expansion coefficients of GaAs ($6.4 \times 10^{-6}/K$)

and Si $(2.4 \times 10^{-6}/K)$.

The first problem would lead to a low minority carrier lifetime[9] and poor morphology.[10] This problem (APD generation) has been already solved by the use of nominally (100)-oriented Si substrates with a slight misorientation between 2 and 4° towards the [011] direction.[10, 17-20] This effect is accomplished through the formation of a (100) Si surface with a large density of double-atomic-layer steps on the Si surface as a result of the heat treatment of the misoriented Si substrate. The dislocations and surface rough caused by lattice mismatch can be decreased by inserting thin intermediate layer such as GaP, strained-layer superlattices GaAsP/GaAs[21, 22] and InGaAs/GaAs.[23, 24] Figure. 3.1 shows the relationship between lattice constants and thermal expansion coefficients at 300 K for various semiconductor materials. Among many III-V compound, the lattice constant of GaP is almost the same as that of Si (lattice mismatch value is about 0.36% at room temperature) and a dislocation-free GaP layer on Si with a smooth surface had been obtained.[25, 26]. It has been reported the critical thickness for misfit dislocation generation is 90 nm.[26] In order to apply the GaP/Si heterojunction for the devices, detained material parameters such as stress and thickness should be evaluated for the further development of these devices. Usually, the stress of GaP layer grown on Si is investigated by, for example, the double-crystal X-ray diffractometer (DXD) technique, photoluminescence (PL), and Raman spectroscopy (RS). However, these methods cannot be used for the evaluation of thin GaP on Si. A GaP layer thinner than the critical thickness is too thin to be evaluated by DXD or RS. Moreover, PL intensity of a thin GaP layer is very weak. Until now, only a little work has been done on thin GaP layer grown on Si substrate. Recently, optical properties of strained $Si_{1-x}Ga_x$ alloys layer on Si and $In_xGa_{1-x}As$ on GaAs determined by using Spectroscopic ellipsometry (SE) have been reported[32, 33]. The difference between the strained and relaxed SE spectra have been presented.

The latter two problems would lead to the reduced minority carrier lifetimes[11] and severe bowing of the GaAs/Si wafer which introduces microcracks[12-15] of the GaAs layer on Si. Thermally induced stress also enhances the migration of dislocations.[16, 39] In order to improve crystal quality and surface morphology, great efforts including the use of two-
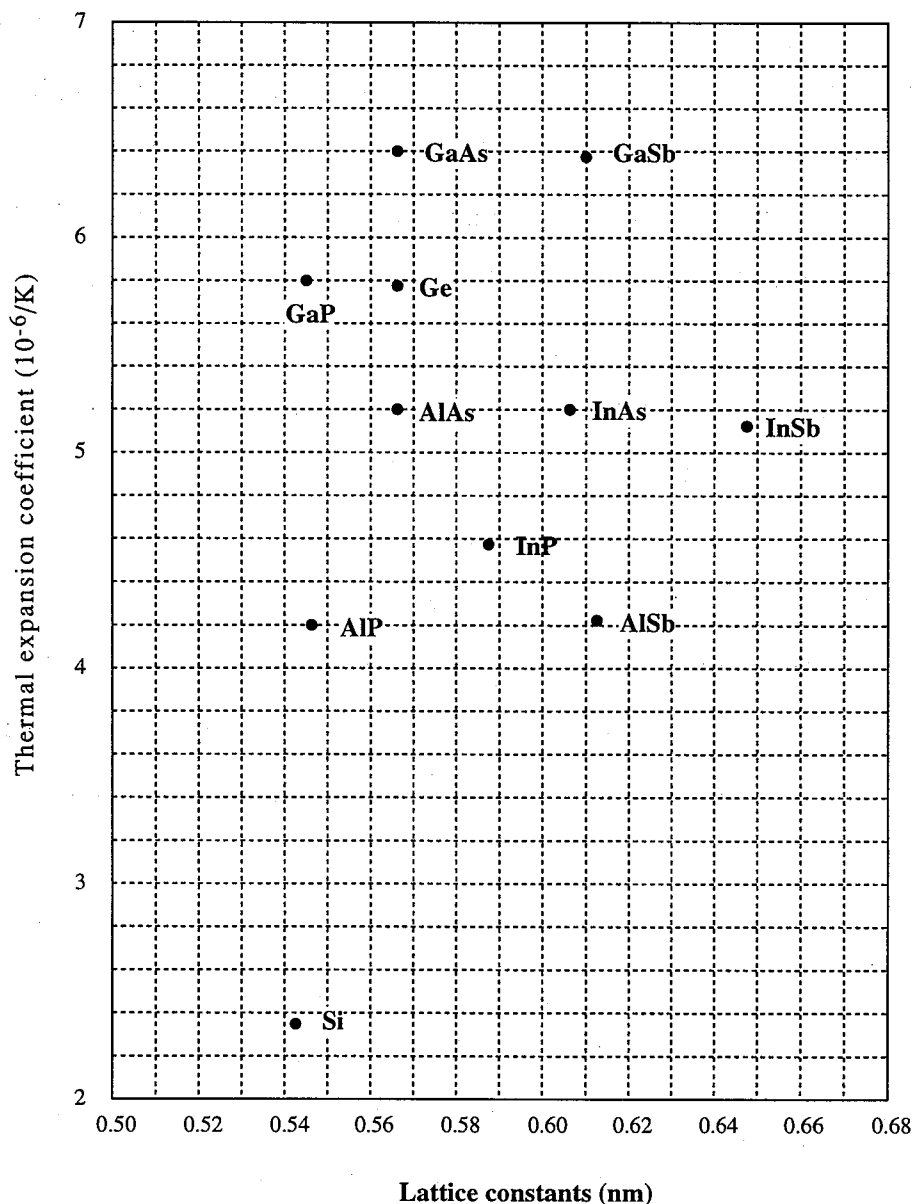
Figure 3.1: Relationship between lattice constants and thermal expansion coefficients at 300 K for various semiconductor materials.

step-grown GaAs/Si using $Al_{0.5}Ga_{0.5}As/Al_{0.55}Ga_{0.45}P$ intermediate layers (AlGaAs/AlGaP ILs)[40] and the four-step-grown technique[41] have been made. Recently, Ohori et al.[42] proposed a novel three step process to improve the surface morphology of GaAs; growth of GaAs on Si substrates by a standard 2-step method, slight (~ 1 μm) mechanochemical polishing, and regrowth of selectively doped heterostructures. The surface roughness was reduced to approximately 1/10 that obtained using conventional methods.

Spectroscopic ellipsometry (SE) is a nondestructive and highly sensitive technique to in-

vestigate optical response of both solid and film and for the quantitative determination of thin film thickness. It has been widely used to determine semiconductor's physical parameters, such as band-structure, stress and alloy compositions etc.[27-30] It is also a sensitive method for the evaluation of crystalline quality and surface morphology [43,44]. Recently, Rossow et al. judged the quality of MBE grown GaAs on Si substrate by SE. It was proposed that the height of the imaginary part of dielectric function at E_1 and $E_1+\Delta_1$ band energy represent the crystalline quality.[45] Moreover, the ellipsometry-derived pseudodielectric function ε_2 of semiconductors, at the E_2 peak wavelength, provides a sensitive indication of the presence of surface oxides, microstructures and damaged surfaces.[31,46] However, in order to investigate the surface characteristics of a material using an effective medium approximation (EMA), it is necessary to know the intrinsic dielectric function of that material. It has been shown that a "bare" surface can be obtained by chemomechanical polishing and chemical etching.[47,48] Atomic force microscopy (AFM) is an important technique for studying surface morphology. Several authors have already employed both SE and AFM to study Si surfaces[49,50] and chemical-mechanical polished GaAs substrate surfaces.[51]

In this chapter, it is described that the characterization of extremely flat GaP layers grown on Si by using SE. A new way of analysis using interband transitions (critical point) for GaP and Si has been developed in order to determine the stress and thickness of the epitaxial layer. The fitting of the experimental SE spectrum to the theoretical SE spectrum by taking account of the effect of strain (ΔE_1) on the critical points E_1 of GaP and Si (E_1). The variation of E_1 transition energy in the GaP and Si with varying thickness of GaP layer is described.

Two evaluative methods have been proposed. i) SE measured data is analyzed by the harmonic oscillator model to characterize the highest crystalline quality among the various intermediate layer, ii) before the evaluation by SE and AFM the chemical polishing of GaAs on Si is used to minimize degree of microroughness of the surface. The rms roughness values are typically 0.3 nm for polished surfaces and the maximum $\varepsilon_2(E_2)$ values are ~24.5 for polished samples, which compares well to the maximum value of 25.22 obtained from

Br$_2$ in methanol (BrM) treated bulk GaAs.[47] The depth of surface roughness for unpolished samples using the obtained dielectric function of polished samples, and the excellent agreement with the root-mean-square (rms) values obtained by AFM are discussed in the following.

3.2 The analysis for GaP/Si strained heterostructure

3.2.1 Experimental

GaP was grown on a Si substrate by conventional low-pressure metalorganic chemical vapor deposition (MOCVD). The growth conditions are almost the same as those reported previously. [26] The orientation of the substrate is (001) tilted [111] by 4°. The source materials for Ga and P are trimethylgallium and PH$_3$, respectively. The growth temperature, the V/III ratio and the gas pressure are 900°C, 1600 and 380 torr, respectively, which have been optimized in laboratory. GaP grows on Si two-dimensionally from the beginning of the growth under these conditions. The GaP thickness was changed from 10 nm to 50 nm. It has been shown that the surface is extremely flat by transmission electron microscopy (see ref. 26). Since the critical thickness for GaP on Si above which the misfit dislocation is generalized is 90 nm, no dislocations are observed in any of the samples evaluated in this study. Ellipsometry measurement was performed using a variable-angle-of SE (Photo Device Co.Lth). The Ψ (amplitude ratio tanΨ), Δ (phase difference) spectra were recorded as a function of wavelength in the range 300 - 450 nm with a spacing of 5 nm at incident angle of incidence 72°. Spectra were analyzed based on a data base of reference dielectric function for GaP[34] and GaPO[35] which are available in the literature. The unknown parameters can be determined so that the mean square error MSE function is minimized. The MSE function is expressed as,

$$MSE = \frac{1}{N} \sum_{i=1}^{N} \left\{ \left(\Psi_i^{calc} - \Psi_i^{exp} \right)^2 + \left(\Delta_i^{calc} - \Delta_i^{exp} \right)^2 \right\} \tag{3.1}$$

where the Ψ^{calc} and Δ^{calc} indicate the theoretical values of Ψ and Δ, respected, and N is the number of data points.

3.2.2 Theoretical model

The dielectric function $\varepsilon(hv)$ of GaP and the Si substrate is approximated by the critical points (CP's) model as follows:

$$\varepsilon = C + \sum_j A_j \exp(i\Phi_j)(hv - E_j + i\Gamma_j)^{l_j} \tag{3.2}$$

$$\frac{d\varepsilon^2}{d(hv)^2} = \begin{cases} \sum_j n(n-1)A_j e^{i\Phi_j}(hv - E_j + i\Gamma_j)^{n-2}, & for\ n \neq 0 \\ A_j e^{i\Phi_j}(hv - E_j + i\Gamma_j)^{-2}, & for\ n = 0 \end{cases}, \tag{3.3}$$

where C is a constant, A is the amplitude, Φ is the phase angle, E_j is the threshold energy, and Γ is broadening. The exponent n has the value of -1/2 for 1D CP's, 0 for 2D CP's, and 1/2 for 3D CP's. Discrete excitons are represented by n_j=-1.[36] It was been found that, in the given region, $\frac{d\varepsilon^2}{d(hv)^2}$ can be fitted only one CP's at room temperature. It is suggested that the dielectric function $\varepsilon(e)$ of a crystal with strain e is expressed as below using the unstrained value:

$$
\begin{aligned}
\varepsilon(e) = C \ &+ \ \sum_{j \neq 1} A_j e^{i\Phi_j}(hv - E_j + i\Gamma_j)^n \\
&+ \ A_1 e^{i\Phi_1}(hv - E_1 + i\Gamma_1)^n \tag{3.4}
\end{aligned}
$$

$$
\begin{aligned}
C \ &+ \ \sum_{j \neq 1} A_j e^{i\Phi_j}(hv - E_j + i\Gamma_j)^n \\
&+ \ A_{10} e^{i\Phi_{10}}(hv - E_{10} + i\Gamma_{10})^n \\
&+ \ e^{i\Phi_{10}}(hv - E_{10} + i\Gamma_{10})^n \Delta A_1 \\
&+ \ iA_{10} e^{i\Phi_{10}}(hv - E_{10} + i\Gamma_{10})^n \Delta\Phi_1 \\
&- \ nA_{10} e^{i\Phi_{10}}(hv - E_{10} + i\Gamma_{10})^{n-1} \Delta E_1 \\
&+ \ inA_{10} e^{i\Phi_{10}}(hv - E_{10} + i\Gamma_{10})^{n-1} \Delta\Gamma_1 \tag{3.5}
\end{aligned}
$$

$$
\begin{aligned}
= \varepsilon(0) \ &+ \ e^{i\Phi_{10}}(hv - E_{10} + i\Gamma_{10})^n \Delta A_1 \\
&+ \ iA_{10} e^{i\Phi_{10}}(hv - E_{10} + i\Gamma_{10})^n \Delta\Phi_1 \\
&- \ nA_{10} e^{i\Phi_{10}}(hv - E_{10} + i\Gamma_{10})^{n-1} \Delta E_1 \\
&+ \ inA_{10} e^{i\Phi_{10}}(hv - E_{10} + i\Gamma_{10})^{n-1} \Delta\Gamma_1 \tag{3.6}
\end{aligned}
$$

where $\varepsilon(0)$ is the dielectric function without strain, A_{10}, Φ_{10}, E_{10} and Γ_{10} are the values of parameter A_1, Ψ_1, E_1 and Γ_1 without, the ΔA_1, $\Delta\Psi_1$, ΔE_1 and $\Delta\Gamma_1$ are the variations

of A_1, Ψ_1, E_1 and Γ_1 due to a strain e, respectively. In order to determinate A_{10}, Φ_{10}, E_{10} and Γ_{10}, it was numerically calculated that the second derivative of the ε of GaP (Fig. 3.2 circles) and Si (Fig. 3.3 circles) using ε of GaP substrate and Si substrate from literature.[34] The calculated and experimental dielectric curves are shown in Fig. 3.2 and Fig. 3.3, respectively. It is shown that the experimental curves are fitted to the calculated ones well. The E_1 values of Si and GaP obtained by this fitting are 3.37 eV and 3.69 eV, respectively which are in good agreement with the values determined by P.Lautenschlager et al.[36] and Stefan Zollner et al.[37]
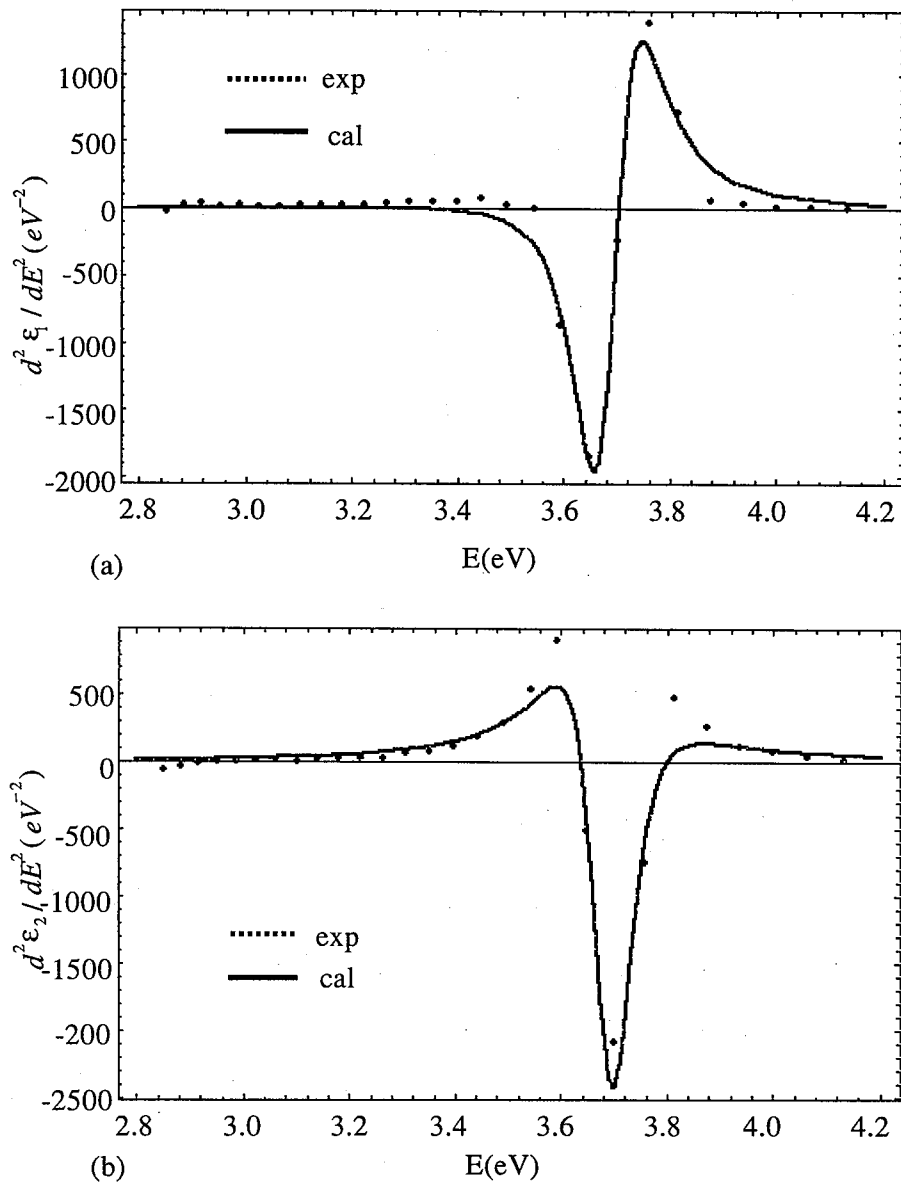

Figure 3.2: Numerically calculated second derivatives of ε_1 (a) and ε_2 (b) for GaP, together with the fitting of eq. (3.3).
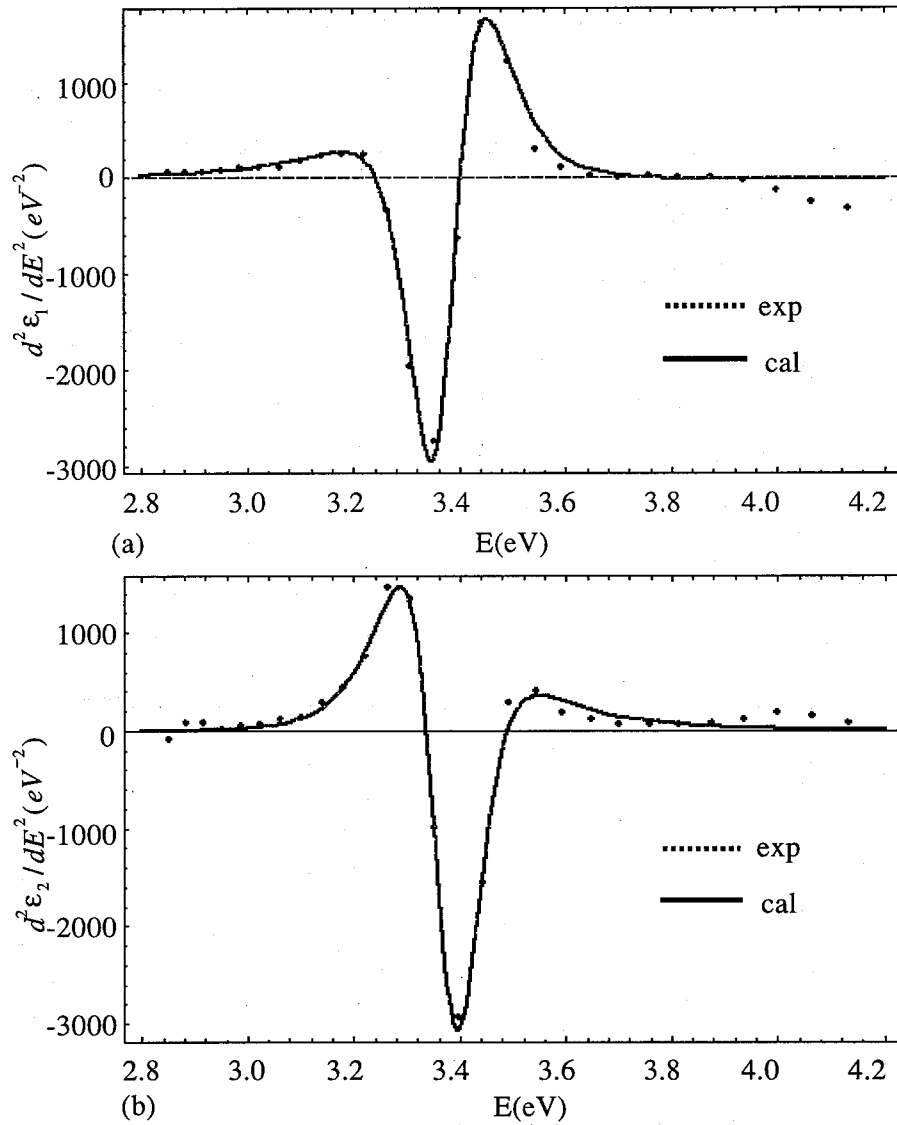
Figure 3.3: Numerically calculated second derivatives of ε_1 (a) and ε_2 (b) for Si, together with the fitting of eq. (3.3)

3.2.3   Results and discussion

The model used to determine the parameters of GaP and Si is shown in Fig 3.4. It consists of a Si substrate, GaP layer (thickness t_2) and GaP oxide layer (thickness t_1). To analyze the measurements, the dielectric function ε_1 of the GaP layer and Si substrate was approximated by eq. 3.6. ΔA_1, $\Delta \Psi_1$, ΔE_1 and $\Delta \Gamma_1$ of GaP and Si, and the thicknesses t_1 and t_2 are variables in the calculation. The fitting results of SE filling curves (Δ and Ψ) for various GaP thicknesses are shown in Fig. 3.5 3.7(sample (A), (B) and (C), respectively). The surface roughness was not taken into account in the calculation since the TEM analysis

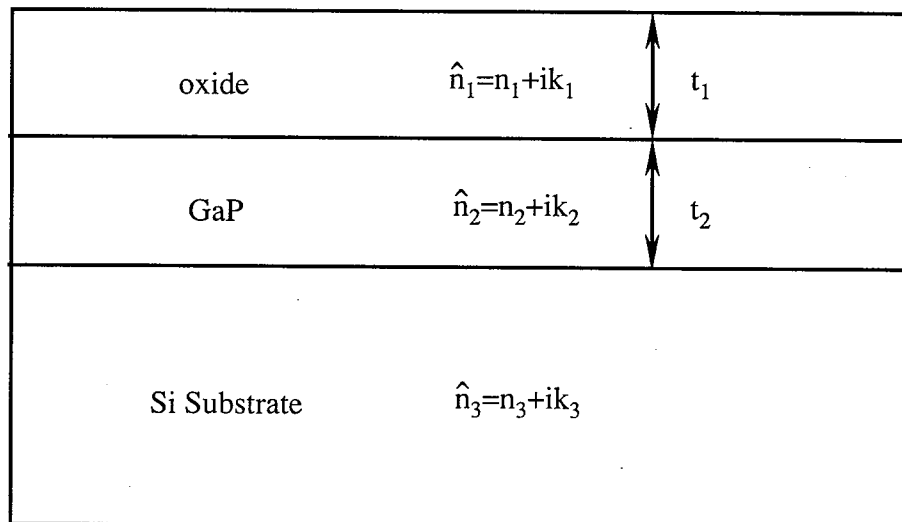| oxide | $\hat{n}_1 = n_1 + ik_1$ | t_1 |
| GaP | $\hat{n}_2 = n_2 + ik_2$ | t_2 |
| Si Substrate | $\hat{n}_3 = n_3 + ik_3$ | |

Figure 3.4: Model of the GaP/Si structure used for SE data analysis.

Table 3.1: GaP oxide thickness and GaP thickness measured by SE and TEM for various samples.

Sample	GaP oxide thickness (nm)	GaP thickness (nm)	
		SE	TEM
A	3.5	8.9	8.0
B	4.5	26.1	22.7
C	2.7	53.1	55.7

Table 3.2: The value for various parameters of the GaP layer and substrate for different of the GaP layer.

Sample	GaP				Si			
	ΔA_1	$\Delta \Psi_1$ (rad)	ΔE_1	$\Delta \Gamma_1$ (eV)	ΔA_1	$\Delta \Psi_1$ (rad)	ΔE_1	$\Delta \Gamma_1$ (eV)
A	-0.047	0.032	0.02	0.042	0.562	0 (fixed)	-0.027	0 (fixed)
B	-0.173	-0.014	0.016	0.021	2.107	0 (fixed)	-0.026	0 (fixed)
C	-0.225	-0.006	0	0.016	0.281	0 (fixed)	-0.011	0 (fixed)

showed the surface to be very smooth (see ref. 26). The GaP layer and oxide thicknesses are listed in Table 3.1. The GaP layer thickness measured by cross-sectional transmission electron microscopy (TEM) are also shown. The results from TEM are in good agreement with those from SE. ΔA_1, $\Delta \Psi_1$, ΔE_1 and $\Delta \Gamma_1$ of GaP and Si for samples (A), (B) and
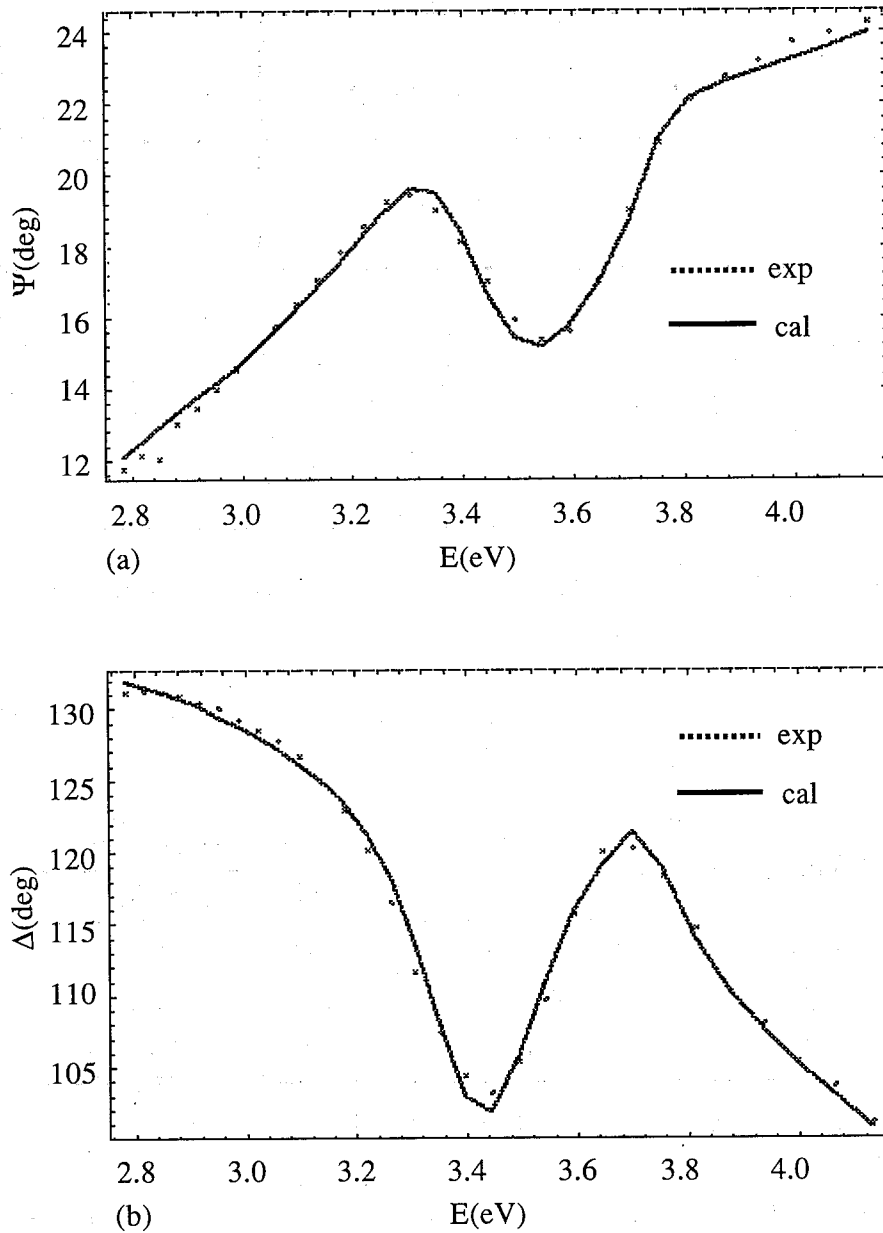
Figure 3.5: Measured (dotted line) and fitted (solid line) (a) Ψ and (b) Δ curves for sample A (GaP thickness is 10 nm).

(C) are listed in Table 3.2. The value of ΔA_1 for GaP increase and the value of $\Delta \Gamma_1$ for GaP decreases with increasing thickness of the GaP layer. Figure 3.8 shows the variation of E_1 from the bulk value (ΔE_1) for the GaP layer and Si substrate as a function of the GaP layer thickness. The explanation of the strain for the GaP/Si heterostructure and lattice relaxation mechanism are discussed. The band-gap energy of GaP shifts towards the high-energy side because of the compressive stress due to the lattice mismatch. On the other hand, tensile strain is applied to the Si substrate. These results coincide with the
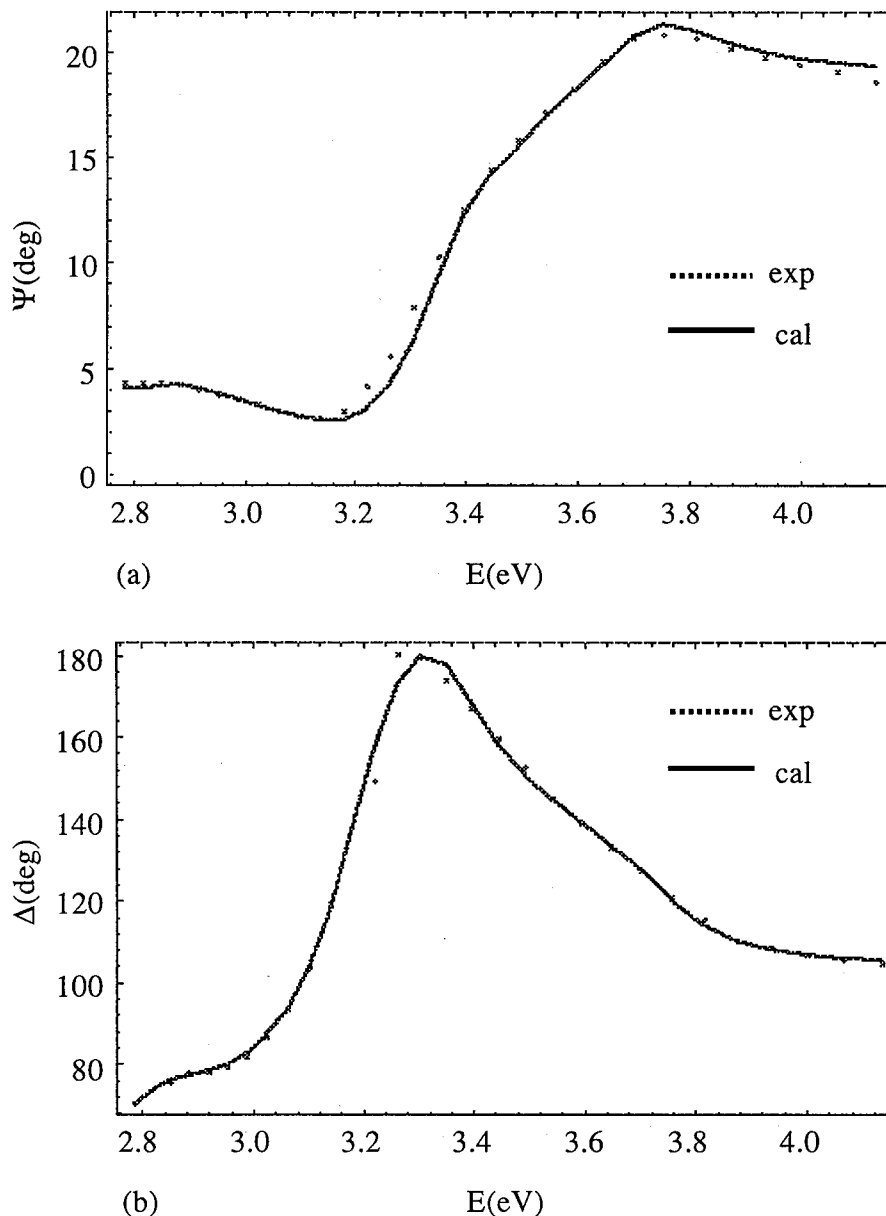
Figure 3.6: Measured (dotted line) and fitted (solid line) (a) Ψ and (b) Δ curves for sample A (GaP thickness is 20 nm).

TEM results that dislocations are not detected.[26] The lattice constant of GaP is slightly larger than that of Si. The interesting feature in Fig. 3.8 is that the compressive stress of GaP and the tensile stress of Si decrease gradually with increasing thickness and that the stress of the 50 nm-thick GaP layer grown on Si is almost zero.

It is well known that misfit stress caused by lattice mismatch is relaxed by introduction of misfit dislocations beyond the critical thickness.[38] However, the lattice mismatch of GaP and Si evaluated in this study is relaxed by deformation of the lattice since no dislocation is
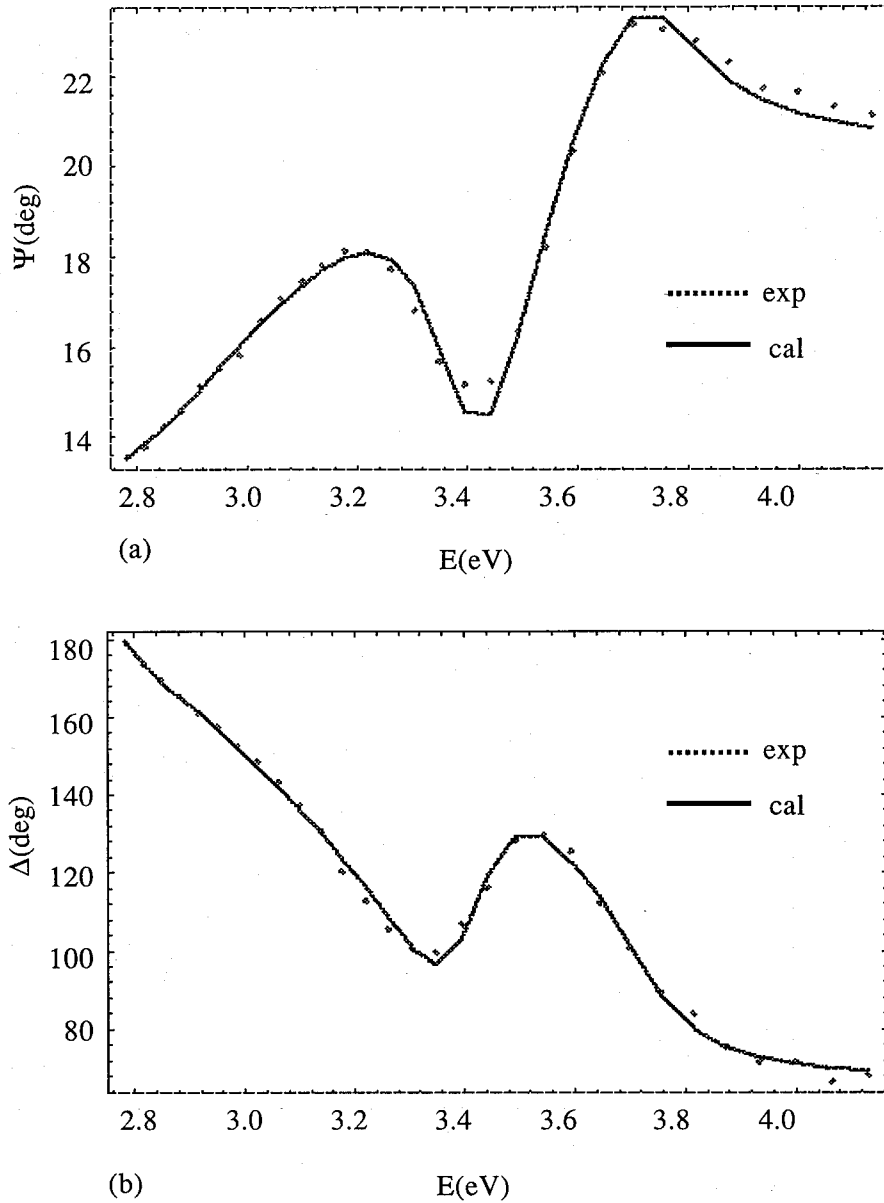
Figure 3.7: Measured (dotted line) and fitted (solid line) (a) Ψ and (b) Δ curves for sample A (GaP thickness is 50 nm).

observed in any of the samples. If the lattice constant of GaP layers parallel to the interface coincides with that of Si for various thicknesses, ΔE_1 should be constant. However, this is not the case here. We propose lattice relaxation mechanisms for GaP on Si to explain the experimental results. When the GaP layer thickness is sufficiently thinner than the critical thickness, lattice mismatch is accommodated by homogeneous elastic stress. The lattice constant parallel to the interface coincides with that of Si. Therefore, δE_1 becomes large. When the layer thickness is increased and approaches the critical thickness, the shape of
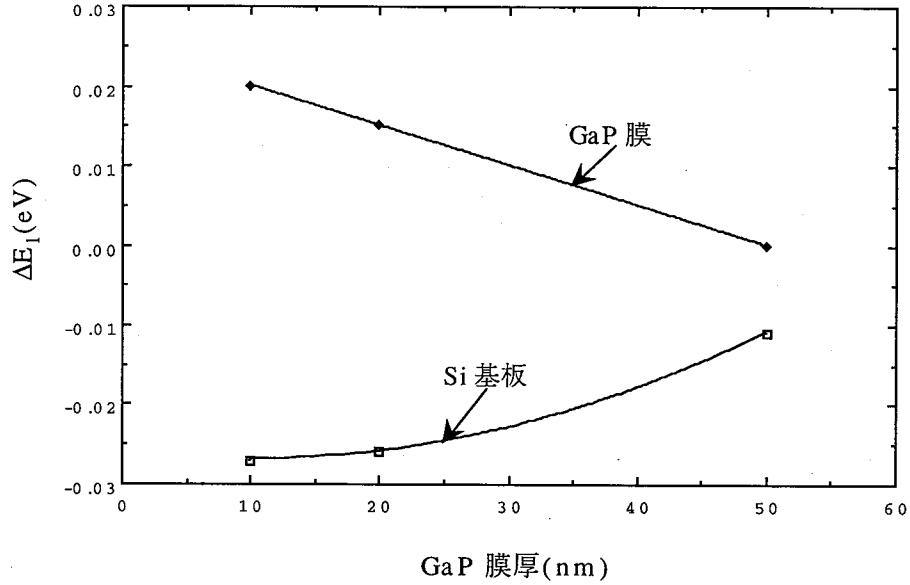
Figure 3.8: Thickness dependence of ΔE_1 for GaP layer and Si substrate.

the lattice near the surface approaches the bulk value in order to relax lattice mismatch without introducing misfit dislocation. Therefore, ΔE_1 decreases with thickness, which is due to the inhomogeneous stress distribution in the layer. Misfit dislocations are generated in order to relax lattice mismatch when the layer thickness exceeds the critical thickness.

3.3 Study on GaAs films grown on Si substrate with several intermediate layers

3.3.1 The evaluation of crystalline quality by harmonic oscillator approximation model

Experiment

GaAs was grown on a Si substrate with intermediate layers GaP and AlGaP by an ordinary MOCVD. GaAs/GaAs$_{0.5}$P$_{0.5}$ (20 nm, 10 layers) strained layer superlattice (SLS) was grown to reduce the dislocation density. The orientation of the Si substrate is (001) tilted toward [110] by 2°. The thicknesses of GaAs layer is 3 μm. The intermediate layer structure, grown temperature and dislocation density revealed by molten KOH are listed in Table 3.3.

Ellipsometry measurement was performed at an incident angle of 70°. The Ψ (amplitude

Table 3.3: The grown conditions and dislocation density.

Sample	Intermediate layer	Growth temperature °C	Dislocation density ($\times 10^7$ cm^{-2})
A	AlGaP+SLS	750	1
B	AlGaP	700	3
C	GaP	700	7

ratio: tanΨ), and Δ (phase difference) spectra were recorded as a function of wavelength in the range of 326 - 460 nm with a spacing of 2 nm. Spectra were analyzed based on a database of reference dielectric function for GaAs and GaAsO which are available in the literature.

Results and discussion

Erman et al. had proposed that the dielectric function of bulk GaAs can be expressed by sum of seven harmonic oscillators in the photon energy region of 1.5 - 6 eV,[45] the form is as following:

$$\varepsilon = C + \sum_{i=1}^{7} A_i \left(\frac{1}{E + E_i + i\Gamma_i} - \frac{1}{E - E_i + i\Gamma_i} \right), \tag{3.7}$$

where i is the index for a particular oscillator, A_i is the amplitude, E is the photon energy, E_i is the center energy of the oscillator, and Γ_i is the oscillator broadening coefficient. It is found that, in the wavelength range of vicinity of E_1 and $E_1+\Delta_1$, the only variation of parameters of two harmonic oscillators corresponding to transitions about E_1 and $E_1+\Delta_1$ can satisfactorily fit on measured SE data. These parameters can represent the variation of dielectric function originating from the crystalline quality and stress. In order to evaluate the surface roughness of overlayer, a three-phase mode (GaAs oxide/(GaAs + Void)/GaAs) had been used. The void in top layer (GaAs oxide layer) was ignored because the refractive index of GaAs oxide is nearly that of void (n=1). Moreover, the penetration depth of light in GaAs decreases from 250 nm at $h\upsilon$=2 eV to 5 nm near the E_2 band energy,[45] the substrate Si can be ignored in the fitting. The effective dielectric function of rough layer
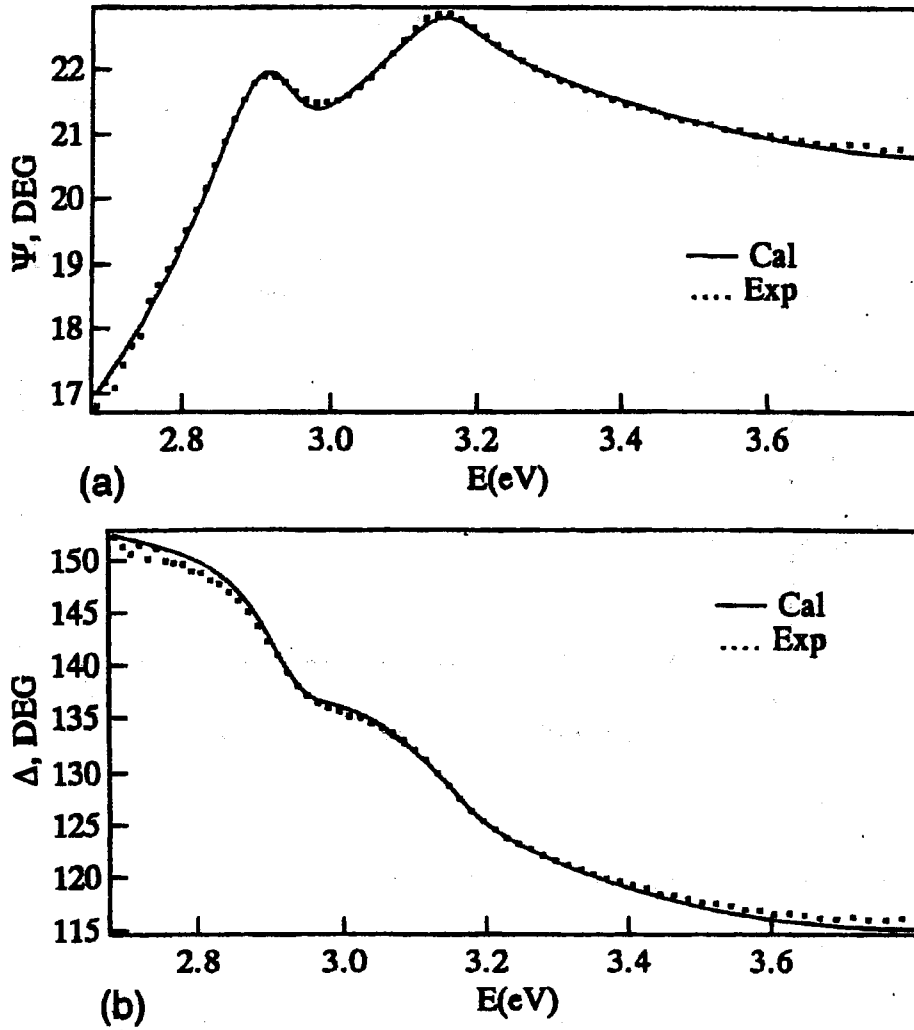
Figure 3.9: Measured (dotted line) and fitted (solid line) (a) Ψ and (b) Δ curves for sample A.

is represented by the Bruggeman effective-medium approximation (EMA).[52] The form is as following:

$$0 = f_v \frac{\varepsilon_v - \varepsilon}{\varepsilon_v + 2\varepsilon} + f_b \frac{\varepsilon_b - \varepsilon}{\varepsilon_b + 2\varepsilon} \tag{3.8}$$

where ε, ε_v and ε_b are the effective complex dielectric function of layer, dielectric function of void and bulk material, respectively. f_v and f_b represent the volume fraction of void and bulk material.

The parameters of two harmonic oscillators, together with two thickness (t_1 and t_2) and

volume fraction of the rough-surface overlayer, were determined so that the mean square error (MSE) function is minimized. MSE function is expressed as:

$$MSE = \frac{1}{N} \sum_{i=1}^{N} \left\{ \left(\tan \Psi_i^{exp} - \tan \Psi_i^{cal} \right)^2 + \left(\cos \Delta_i^{exp} - \cos \Delta_i^{cal} \right)^2 \right\} \qquad (3.9)$$

where the Ψ_i^{cal} and Δ_i^{cal} indicate the theoretical values of Ψ and Δ, respectively, and N is the number of data points.
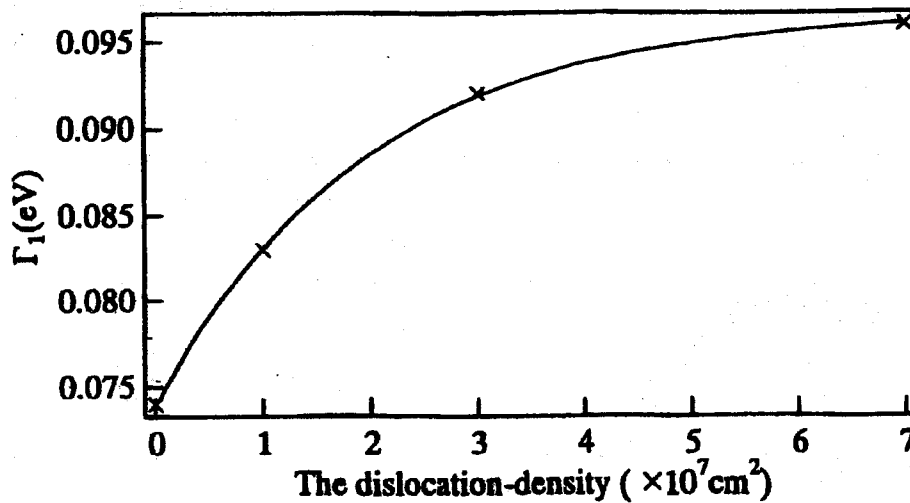

Figure 3.10: DepHndnece of oscillator broadening coefficient Γ on the dislocation-density for GaAs layer on Si.

The fitting curve for one typical sample is shown in Fig. 3.9. As clearly seen in the figure, model results are in excellent quantitative agreement with experimental data. All the parameters obtained by fitting are listed in Table 3.4. The center energies of the oscillator E_1 of GaAs layers for all samples shifted toward low energy side about same value from that of bulk GaAs, which indicates that the tensile stress is applied to GaAs layer and the stress value is about the same for various intermediate layer structure. It is also clear that the surface roughness greatly depend on the intermediate layer structure. The surface roughness of GaAs on Si with AlGaP intermediate layer is smallest, which is consistent with the TEM observation.[53] Since the broadening parameter Γ_1 arises mainly from lattice defects, it can be used to judge the crystalline quality of layer. In Fig. 3.10, Γ_1 for GaAs layer is plotted as a function of dislocation density. Because Γ_1 increases at high dislocation den-

Table 3.4: Chemical treatments yielding the sharpest dielectric discontinuity between bulk and ambient.

Parameter	Sample			
	bulk GaAs	A	B	C
A_1	0.6324	0.6757	0.7127	0.7947
E_1 (eV)	2.9188	2.9065	2.9067	2.9093
Γ_1 (eV)	0.0739	0.0833	0.0921	0.0963
A_2	1.4113	1.5251	1.5499	1.3210
E_2 (eV)	3.1130	3.1054	3.1061	3.114
Γ_2 (eV)	0.1611	0.1701	0.1774	0.1573
d_1 (nm)		3.562	5.204	2.342
d_2 (nm)		0.778	0.8023	2.892
f_a		0.206	0.218	0.341

sity, the spectroscopic ellipsometry is a good nondestructive method to evaluate the crystal quality. This figure indicates that GaAs on Si substrate with AlGaP+SLS intermediate layer reaches the highest crystalline quality among the experimental samples.

3.3.2 Effect of NaOCl-Polishing on GaAs surface on Si substrate by SE and AFM

Experiment

GaAs layer was grown on a Si substrate with intermediate layers of GaP, AlGaP and GaAsP using conventional metal organic chemical vapor deposition (MOCVD). A GaAs /$Al_{0.5}Ga_{0.5}As$ and GaAs/$GaAs_{0.5}P_{0.5}$ (20nm, 10 layers) strained layer superlattice (SLS) intermediate layers were respectively used in sample 1 and 4 to reduce the dislocation density of GaAs layer as shown in Table 3.5. The orientation of the Si substrate is (100) tilted toward [110] by 2°. The thicknesses of GaAs layers for various samples, the intermediate layer structure and growth temperature are listed in Table 3.5. Sample surfaces were treated by chemomechanical polishing for 1 min with NaOCl, followed by NH_4OH polishing for 30 s and a rinsing with water.

Table 3.5: Nature of intermediate layer, growth temperature and thickness of GaAs top layer for various samples.

Sample No.	Intermediate layer	Growth temperature (°C)	Thickness of GaAs (μm)
1	AlGaP+SLS	750	3
2	AlGaP	750	3
3	AlGaP	700	3
4	GaAsP+SLS	750	3
5	GaAsP	750	3
6	GaAsP	750	3
7	GaP	750	3

All SE measurements were performed at room temperature over the wavelength range of 250~830 nm with a step of 5 nm at a 70° angle of incidence. The samples were maintained in a dry N_2 flow during the measurements to eliminate surface contamination effects. The effect of the attenuation of the ac component of the measured signal was taken into account.[54] AFM was employed to measure the surface roughness of the polished samples and unpolished samples. The rms roughness was computed from 5×5 μm scans.

Results and discussion

The pseudodielectric function is derived from the SE data assuming the sample is perfectly abrupt and overlayer-free. The cleaved surface, in general, is thought to be closest to no overlayer(s) realistic surface.[55] Therefore, we measured SE spectrum of the GaAs cleaved surface in a dry N_2 flow, and the pseudodielectric function spectrum is shown in Fig. 3.11 (dashed line). In the same figure we also show the pseudodielectric-function spectra of GaAs grown on Si both in the as-grown state (solid line) and after polishing (dotted line). Figure 3.11 reveals that our chemical treatment results in a maximum ε_2 of 24.5 at the E_2 peak (E~4.77 eV) for GaAs on Si which compares well to the maximum value for BrM-treated bulk samples.[47] The peak broadening difference of ε_2 between cleaved and polished surface near the E_1 (3.0 eV) arises from the crystalline quality and doping level of the layer.[56,57]

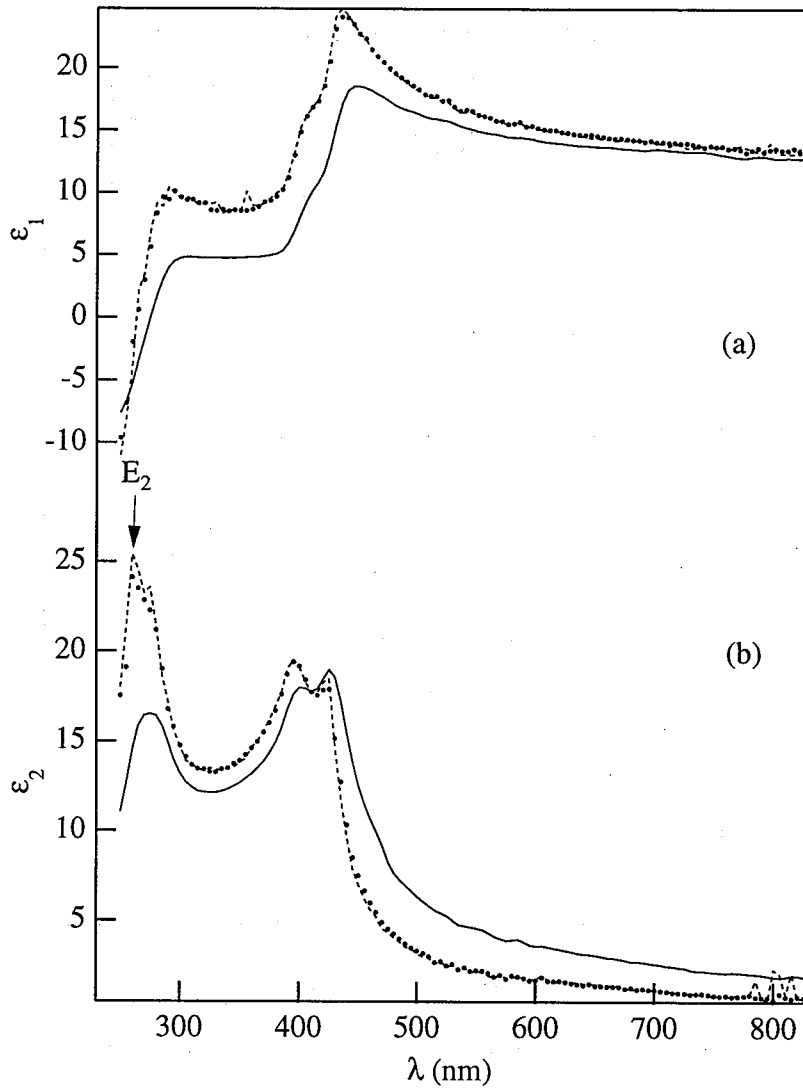Figure 3.11: ε_1 (a) and ε_2 (b) spectra of sample 1 before (solid line) and after (dotted line) polishing. The dashed line represents the spectra of the GaAs cleaved surface.

In order to determine qualitative by the surface roughness of unpolished samples from the measured SE data, we performed the a linear regression analysis (LRA) using EMA and the multilayer model a schematic of which is shown in Fig. 3.12. The Bruggememan EMA can be defined by the following expression[58]

$$0 = \sum_{i}^{n} f_i \frac{\varepsilon_i - \varepsilon}{\varepsilon_i + 2\varepsilon} \tag{3.10}$$

$$1 = \sum_{i}^{n} f_i,$$

where ε_i and f_i are, respectively, the complex dielectric function and the volume fraction of

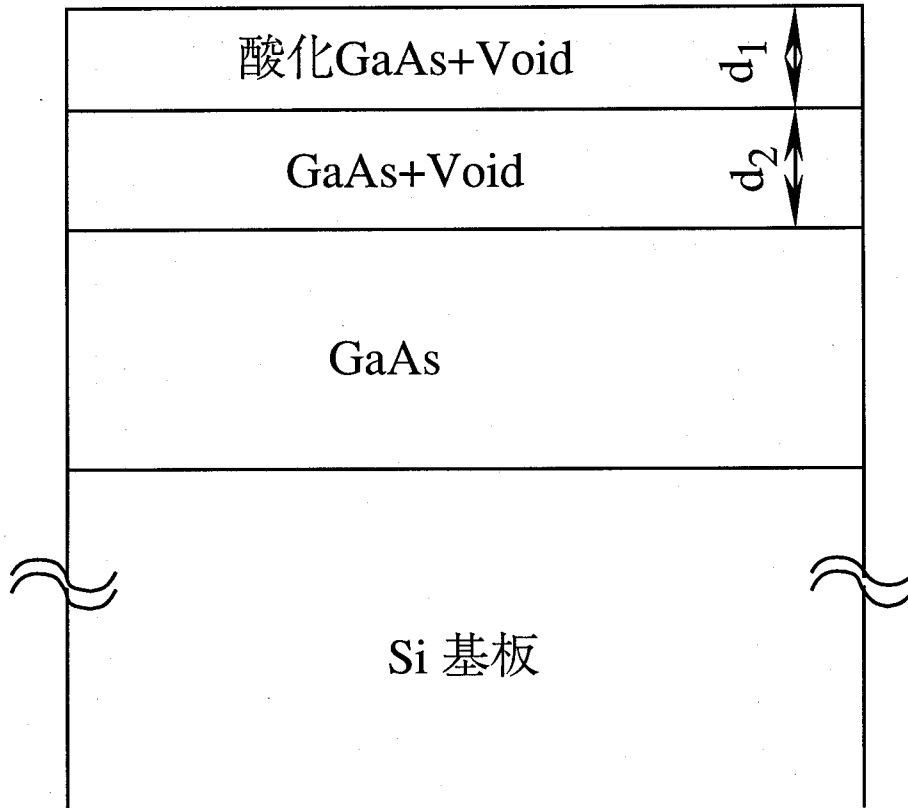|	
酸化GaAs+Void	d_1
GaAs+Void	d_2
GaAs	
Si 基板	

Figure 3.12: Model for SE measurement.

each of the components i, and ε is the complex dielectric function of the film layer studied. The dielectric function $\varepsilon = \varepsilon_1 + i\varepsilon_2$ of void is taken as $\varepsilon = 1$ and the complex dielectric function of oxide GaAs in layer 1 is taken from ref. 59. The dielectric functions obtained from polished samples are used for GaAs in layers 2 and 3. The void fraction f_v in both layers 1 and 2 is assumed to be the same in this work. Therefore, three unknown parameters (d_1, d_2 and f_v) can be numerically determined by minimizing the following mean-square deviation with a regression program

$$\sigma^2 = \frac{1}{N-P} \sum_{i=1}^{N} \left[\left(\Psi_i^{\mathrm{exp}} - \Psi_i^{cal} \right)^2 + \left(\Delta_i^{\mathrm{exp}} - \Delta_i^{cal} \right)^2 \right], \tag{3.11}$$

where N is the number of data points and P is the number of unknown model parameters.

Figure 3.13a and b show the best-fit results of the LRA-EMA analysis for sample 6. The measured SE data are plotted by a dotted line and the LRA-EMA calculation results are shown by a solid line. Very good fits were obtained in both Ψ and Δ spectra over the entire wavelength region. The parameters obtained from this fit are listed in Table 3.6. RMS
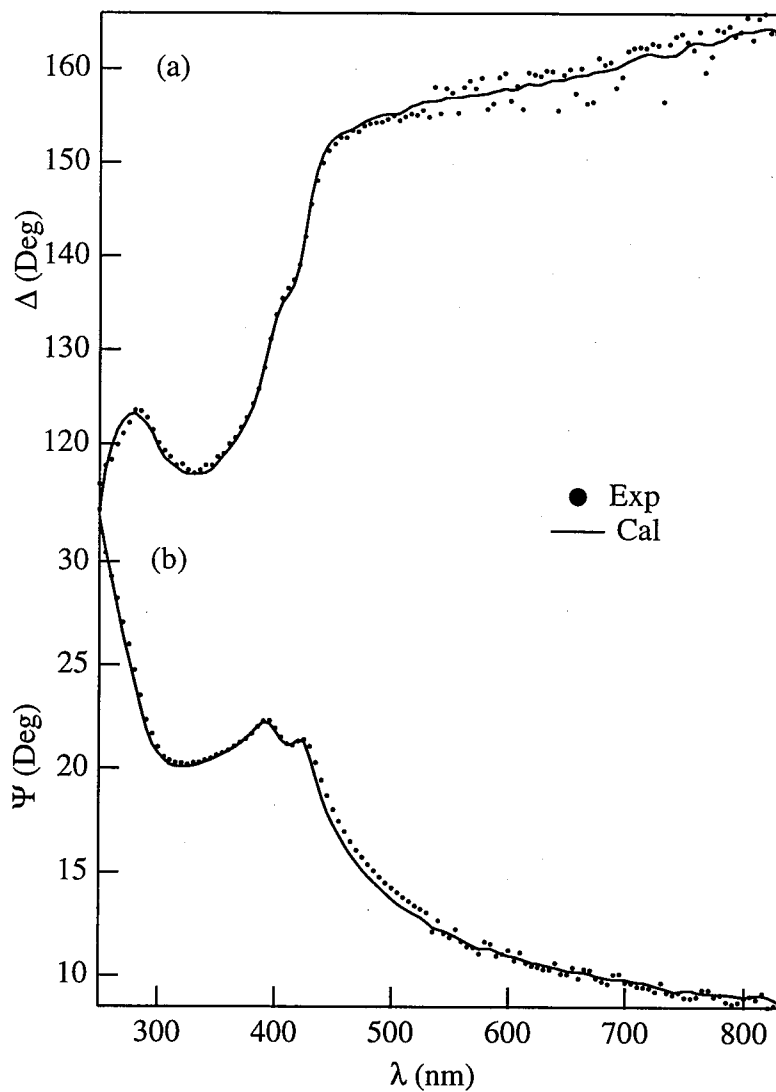
Figure 3.13: Measured (dotted line) and calculated (solid line) Δ (a) and Ψ (b) spectra using the model shown in Fig. 2.

values obtained by AFM are also listed in Table 3.6. It is clear that the surface roughness is considerably different for the various intermediate layer. The lowest degree of surface roughness of GaAs on Si observed for sample 1 and sample 4 with AlGaP SLS or GaAsP SLS, are consistent with previous results.[60, 61]

Figure 3.14 shows the AFM image obtained from the polished (Fig. 3.14b) and unpolished (Fig. 3.14a) surface of sample 1. As expected from the LRA-EMA result, the AFM image clearly indicates that before polishing the sample has a very rough surface with a rms value of 3.44 nm, whereas the surface roughness was greatly reduced by chemical polishing to

Table 3.6: Details of the structural parameters used in SE analysis and standard deviation (rms) used in AFM. The 90% confidence limits are shown by ($\pm$).

Sample No.	SE				AFM rms (nm)
	f_v	d_1(nm)	d_2	δ	
1	0.569$\pm$0.001	1.33$\pm$0.05	1.65$\pm$0.04	0.69	3.44
2	0.386$\pm$0.005	1.61$\pm$0.09	3.87$\pm$0.09	0.98	4.87
3	0.389$\pm$0.001	2.76$\pm$0.02	2.85$\pm$0.02	0.90	5.74
4	0.568$\pm$0.0003	1.40$\pm$0.05	1.50$\pm$0.03	0.77	2.51
5	0.470$\pm$0.001	2.41$\pm$0.05	2.31$\pm$0.04	0.99	3.98
6	0.527$\pm$0.02	2.80$\pm$0.4	1.38$\pm$0.3	0.81	4.87
7	0.270$\pm$0.001	1.50$\pm$0.04	4.17$\pm$0.07	0.93	5.39

give an rms value of 0.34 nm, which is about 1/10 that of the unpolished sample.

In order to compare the results obtained by AFM with the results obtained by SE, we recognized that the depth (d) of the surface roughness obtained by SE is the sum of d_1 and d_2 as shown in Table 3.6. The relationship between d and rms calculated from AFM images is shown in Fig. 3.15. The deviation between data points and the line is very small and in turn indicates that SE measurements agree well with the results obtained by AFM measurements.

3.4   Conclusion

The characterization results of a strained GaP layer grown on a Si substrate by spectroscopic ellipsometry have been described. The band-gap energies of GaP and Si, GaP layer thickness and the GaP oxide layer for a strained GaP/Si heterostructure were determined by the calculated fitting. The compressive stress applied to the GaP layer and the tensile stress applied to the Si substrate decrease gradually with increasing GaP layer thickness in the thickness range less than the critical thickness. The lattice relaxation of GaP occurs gradually with increasing thickness.

The MOCVD-grown GaAs on Si have been investigated by SE. The results obtained from the proposed model indicate that it can be simultaneously determined the thicknesses,
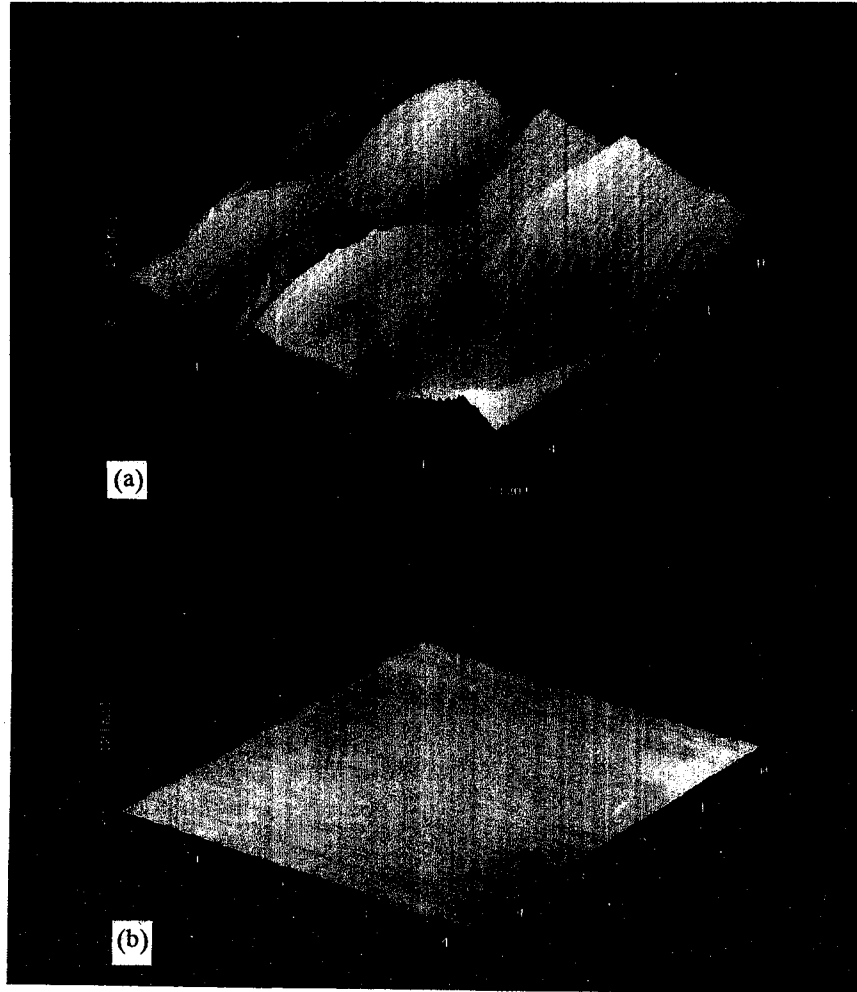
Figure 3.14: AFM images (5×5 μm) of sample 1 taken before (a) and after (b) polishing.

stress and crystalline quality. The tensile stress is applied to GaAs layer and the GaAs on Si with AlGaP+SLS intermediate layer has best surface morphology and crystalline quality. Further, the surface morphology of NaOCl-polished GaAs grown on Si have been measured by SE and AFM. The maximum value of ε_2 ($\sim$4.77eV) is 24.5 and typical rms is 0.3 nm. The depth of surface roughness determined by SE is in agreement with rms roughness obtained by AFM. Therefore, the surface roughness of GaAs on Si can be reduced to 1/10 that in the as-grown state using NaOCl-polishing, and the results of surface characterization by SE are consistent with AFM measurements.
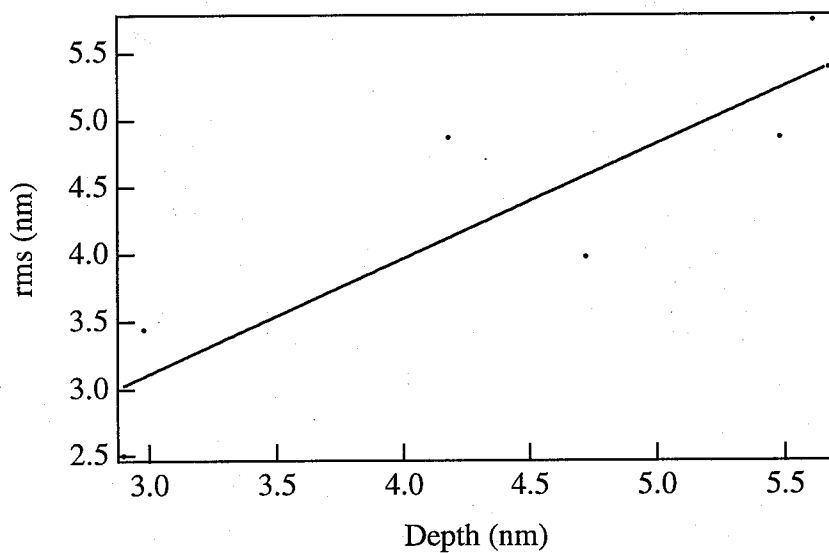
Figure 3.15: A plot of depth of surface roughness obtained by SE vs rms roughness obtained by AFM.

References

[1] H. K. Choi, J. P. Mattia, G. W. Turner and B. Y. Tsaur, IEEE Electron Device Lett., **9**, 512 (1988).

[2] H. Shichijo, R. Matyi, A. H. Taddiken and Y. C. Kao, IEEE Trans. Electron Devices, **37**, 548, 865 (1990).

[3] T. Egawa, T. Jimbo and M. Umeno, IEEE Photon. Technol. Lett., **4**, 612 (1992).

[4] T. Egawa, T. Jimbo and M. Umeno, IEICE Trans. Electron., **E76-C**, 106 (1993).

[5] G. N. Nasserbakht, J. W. Adkisson, B. A. Wooley, J. S. Harris and T. I. Kamins, IEEE J. Solid-State Circuits, **28**, 622 (1993).

[6] I. Hayashi, Jpn. J. Appl. Phys., **32**, 266 (1993).

[7] I. Hayashi, Optoelectron. Devices Technol., **9**, 468 (1994).

[8] K. W. Goossen, J. A. Walker, L. A. D'Asaro, S. P. Hui, B. Tseng, R. Leibenguth, D. Kossives, D. D. Bacon, D. Dahringer, L. M. F. Chirovsky, A. L. Lentine and D. A. B. Miller, IEEE Photon. Technol. Lett,. **7**, 360 (1995).

[9] K. Nauka, G. A. Reid and Z. L. Weber, Appl. Phys. Lett., **56**, 376 (1990).

[10] H. Noge, H. Kano, M. Hashimoto and I. Igarashi, J. Appl. Phys., **64**, 2246 (1988).

[11] R. K. Ahrenkiel, M. M. Al-Jassim, D. J. Dunlavy, K. M. Jones, S. M. Vernon, S. P. Tobin and V. E. Haven, Appl. Phys. Lett., **53**, 222 (1988).

[12] R. W. Kaliski, N. Holonyak, Jr., K. C. Hsieh, D. W. Nam, J. W. Lee, H. Shichijo, R. D. Burnham, J. E. Epler and H. F. Chung, Appl. Phys. Lett., **50**, 836 (1987).

[13] B. G. Yacobi, S. Zemon, P. Norris, C. Jagannath and P. Sheldon, Appl. Phys. Lett., **51**, 2236 (1987).

[14] D. G. Deppe, D. C. Hall, N. Holonyak, Jr., R. J. Matyi, H. Shichijo and J. E. Epler, Appl. Phys. Lett., **53**, 874 (1988).

[15] N. Hayafuji, H. Kizuki, M. Miyashita, K. Kadoiwa, T. Nishimura, N. Ogasawara, H. Kumabe, T. Murotani and A. Tada, Jpn. J. Appl. Phys., **30**, 459 (1991).

[16] M. Tachikawa and H. Mori, Appl. Phys. lett., **56**, 2225 (1990).

[17] S. F. Fang, K. Adomi, S. Iyer, H. Morkoc, H. Zabel, C. Choi, and N. Otsuka, J. Appl. Phys., **68**, R31 (1990).

[18] T. Ueda, S. Nishi, Y. Kawarada, M. Akiyama, and K. Kaminishi, Jpn. J. Appl. Phys., **25**, L789 (1986).

[19] R. Fischer, D. Neuman, H. Zabel, H. Morkoc, C. Choi and N. Otsuka, Appl. Phys. Lett., **48**, 1223 (1986).

[20] S. N. G. Chu, S. Nakahara, S. J. Pearton, T. Boone and S. M. Vernon, J. Appl. Phys., **64**, 2981 (1988).

[21] R. D. Dupuis, and C. J. Pinzone, J. Cryst. Growth, **93**, 434 (1988).

[22] N. Wada, S. Sakai and M. Fukui, Jpn. J. Appl. Phys., **33**, 976 (1994).

[23] S. Adachi, T. Kimura and N. Suzuki, J. Appl. Phys., **74**, 3435 (1993).

[24] T. Egawa, Y. Hasegawa, T. Jimbo and M. Umeno, Jpn. J. Appl. Phys., **31**, 791 (1992).

[25] T. Soga, T. George, T. Suzuki, T. Jimbo and M. Umeno, Appl. Phys. lett., **58**, 2108 (1991).

[26] T. Soga, T. Jimbo and M. Umeno, Jpn. J. Appl. Phys., **32**, L767 (1993).

[27] M. Garriga, M.Cardona, N. E. Christensen, P. Lautenschlager, T. Isu and K. Ploog, Phys. Rev. B **36**, 3254 (1987).

[28] P. Lautenschlager, M. Garriga, L. Vina and M. Cardona, Phys. Rev. B **36**, 4821 (1987).

[29] N. V. Nguyen, K. Vedam and J. Narayan, J. Appl. Phys., **67**, 599 (1990).

[30] R. T. Carline, C. Pickering, D. J. Robbins, W. Y. Leong A. D. Pitt and A. G. Cullis, Appl. Phys. Lett., **64**, 1114 (1994).

[31]

[32] C. Pickering, R. T. Carline, D. J. Robbins, W. Y. Leong, S. J. Barnett, A. D. Pitt, and A. G. Cullis, J. Appl. Phys., **73**, 239 (1993).

[33] C. Pickering, R. T. Carline, N. S. Garawal, L. K. Howard and M. T. Emeny, Appl. Phys. Lett., **60**, 2412 (1992).

[34] D. E. Aspnes and A. A. Studna, Phys. Rev. B **27**, 985 (1983).

[35] D. E. Aspnes, B. Schwartz, A. A. Studna, L. Derick and L. A. Koszi, J. Appl. Phys., **48**, 3510 (1977).

[36] P. Lautenschlager, M. Garriga, L. Viña and M. Cardona, Phys. Rev. B **36**, 4821 (1987).

[37] S. Zollner, M. Garriga, J. Kirchor, J. Humlíčicek and M. Cardona, Thin Solid Film, **233**, 185 (1993).

[38] J. M. Matthews, Epitaxial Growth (Academic Pree, New York, 1975) Part B, p. 559.

[39] T. Egawa, T. Soga, T. Jimbo and M. Umeno: IEEE J. Quantum Electron. **27**, 1798 (1991).

[40] T. Egawa, T. Jimbo and M. Umeno: Appl. Phys. Lett. **61**, 273 (1992).

[41] S. Ohkubo, T. Eshita, S. Miyagaki and K. Takasaki: Inst. Phys. Conf. Ser. **129**, 187 (1993).

[42] T. Ohori, H. Suehiro, K. Kasai and J. Komeno: Inst. Phys. Conf. Ser. **129**, 175 (1993).

[43] K. Utani, T. Suzuki and S. Adachi: J. Appl. Phys. **73**, 3467 (1993).

[44] G. Yu, T. Soga, T. Jimbo and M. Umeno: Jpn. J. Appl. Phys. **34**, 530 (1995).

[45] U. Rossow, T. Fieseler, D. R. T. Zahn, W. Richter, D. A. Woolf, D. I. Westwood and R. H. Williams, Mater. Sci. Eng. B **5**, 309 (1990).

[46] D. E. Aspnes: J. Vac. Sci. & Technol. **17**, 1057 (1980).

[47] D. E. Aspnes and A. A. Studna: Phys. Rev. B: **27**, 985 (1983).

[48] D. E. Aspnes and A. A. Studna: Appl. Phys. Lett. **39**, 316 (1981).

[49] T. Suzuki and S. Adachi: Jpn. J. Appl. Phys. **33**, 5599 (1994).

[50] S. J. Fang, W. Chen, T. Yamanaka and C. R. Helms: Appl. Phys. Lett. **68**, 2837 (1996).

[51] Y. Xiong and P. G. Snyder: Thin Solid Films **220**, 303 (1992).

[52] M. Erman, J. B. Theeten, P. Chambon, S. M. Kelso and D. E. Aspnes, J. Appl. Phys. **56**, 2664 (1984).

[53] N. Noto, S. Nozaki, T. Egawa, T. Soga, T. Jimbo and M. Umeno, Mater. Res. Soc. Symp. Proc. **48**, 247 (1989).

[54] D. E. Aspnes and A. A. Studna: Appl. Opt. **14**, 220 (1975).

[55] F. Lukes: Optik (Stuttgart) **31**, 83 (1970).

[56] M. Erman, J. B. Theeten, N. Vodjdani and Y. Demay: J. Vac. Sci. Technol. **B1**, 328 (1983).

[57] U. Rossow, T. Fieseler, D. R. T. Zahn, W. Richter, D. A. Woolf, D. I. Westwood and R. H. Williams: Mater. Sci. & Eng. **B5**, 309 (1990).

[58] M. Erman, J. B. Theeten, P. Chambon, S. M. Kelso and D. E. Aspnes: J. Appl. Phys. **56**, 2664 (1984).

[59] D. E. Aspnes, G. P. Schwartz, G. J. Gualtieri, A. A. Studna and B. Schwartz: J. Electrochem. Soc. **128**, 590 (1981).

[60] T. Egawa, S. Nozaki, N. Noto, T. Soga, T. Jimbo and M. Umeno: J. Appl. Phys. **67**, 6908 (1990).

[61] N. Noto, S. Nozaki, T. Egawa, T. Soga, T. Jimbo and M. Umeno: Mater. Res. Soc. Symp. Proc. **48**, 247 (1989).

Chapter 4

Polycrystalline Si and $Si_{1-x}Ge_x$ films

4.1 Introduction

Number of applications on low-temperature poly-Si deposited on glass have been reported, including poly-Si TFTs[1] and poly-Si solar cell .[2] Compared with the poly-Si, the $Si_{1-x}Ge_x$ /Si strained-layer heterostructures exhibits more attractive transport and optical properties. The $Si_{1-x}Ge_x$ /Si alloy provides a continuously variable system with a wide range of optical band gaps and polycrystalline SiGe films can be an alternative to poly-Si in several technologies such as thin film transistors (TFTs).[13,14]. Polycrystalline silicon-germanium films are receiving considerable attention for applications such as high speed heterojunction bipolar transistors with the $Si_{1-x}Ge_x$ /Si base formed by high-dose Ge implantation followed by solid phase epitaxy.[12] Crystallization of amorphous silicon and amorphous silicon-germanium alloys, at low temperature, in short time, using excimer laser irradiation has been investigated by several authors.[15,16] The high quality thin film transistors (TFTs) with grain size of about 80 nm[3] and high field-effect mobilities[4] had been made. Furthermore, it is reported that pulsed laser-induced growth of poly-$Si_{1-x}Ge_x$ /Si offers several advantages over alternative epitaxial processes.[17] The heterojunction and quantum well structures of this alloy system also have potential for optoelectronic devices such as modulators, switches and detectors.[18,19] Recently, Nelson et al.[20] have studied the ohmic contacts to n-type silicon-germanium alloys and suggested that an alloy of silver and antimony will be a more reliable metal contact for $Si/Si_{1-x}Ge_x$ /Si n-type heterostructures over the commonly used Au/Sb alloyed contacts.

Spectroscopic ellipsometry (SE) is a very powerful and nondestructive technique to investigate optical response of both solids and thin films. It has been used by several authors to investigate the amorphous-to-crystalline transition of Si films during the growth and thermal annealing.[5,6] Also, spectroscopic ellipsometry (SE) is known as a sensitivity technique to characterize alloys composition. Using SE, Humlicek et al.[21] have produced a series of pseudodielectric ($\varepsilon = \varepsilon_1 + i\varepsilon_2$) functions for a number of bulk $Si_{1-x}Ge_x$ /Si alloys of composition x = 0.22, 0.39, 0.51, 0.64, 0.75, 0.83 and 0.91, and determined the critical point energies by fitting the numerically differentiated dielectric functions. Nguyen et al.[22] have used SE to investigate the properties of the interface between Ge-implanted Si and its thermal oxide and interpreted the data in terms of a $Si_{1-x}Ge_x$ /Si alloy using the measured spectrum of Humlicek et al. SE of strained and relaxed $Si_{1-x}Ge_x$ /Si epitaxial layers of arbitrary compositions were also studied by others.[23,24] However, little work has been done on optical and structural characterization of poly-$Si_{1-x}Ge_x$ /Si alloy thin films for their potential application in opto-electronic devices such as solar cells.

In this chapter, it is presented that optical and surface properties of poly-Si obtained by laser annealing of α-Si, deposited on Si substrate (α-Si/SiO2/Si), by LPCVD, using the cross-sectional transmission electron microscopy (XTEM) and SE. SE measurement shows that the crystallization starts with laser annealing of energy 144 - 280 mJ/cm^2 and above which it remains amorphous.

Further, we propose ion beam sputtering as a simple and convenient method for the deposition of arbitrary compositions of $Si_{1-x}Ge_x$ /Si alloy thin films and excimer laser irradiation for the crystallization of as-deposited films for the future application of Si/SiGe based superlattice structures as solar cell devices. We report the crystal structure, composition and optical properties of both as-deposited and laser annealed films characterized by X-ray diffraction (XRD), uv-visible spectroscopy, auger electron spectroscopy (AES) and SE. We determined the composition of crystallized $Si_{1-x}Ge_x$ /Si thin films using the analysis of the experimental $\varepsilon(\omega)$ with the second-derivative technique. The effect of surface treatment of our films, polished using Syton-saturated lens paper, on optical properties, are studied in terms of critical point (CP) energies strongly depends on the composition of the

alloy system and may be shifted due to the oxidation/roughening.[24] We further discuss the volume fraction of crystalline Si$_{1-x}$Ge$_x$ /Si using the interpolation procedure developed by Snyder et al.[25] and the effective-medium theory (EMT). The dielectric functions of Si$_{1-x}$Ge$_x$ /Si alloys are taken from the literature.[21]

4.2 The properties of excimer laser annealed amorphous -Si/SiO$_2$/Si substrure

4.2.1 Experimental

An SiO$_2$ layer with thickness of about 100 nm is first deposited on Si substrate followed by the deposition done by low pressure chemical vapor deposition (LPCVD) of smooth α-Si thin films with a thickness of about 70 nm. Crystallization was carried out at room temperature and in air using XeCl excimer-laser source of 308 nm wavelength. The irradiation laser energy was varied from 88 to 344 mJ/cm^2. Details concerning the laser irradiation conditions for various samples studied are listed in Table 4.1.

Table 4.1: Laser irradiation conditions for the preparation of poly Si films and their thicknesses. Sample 1 corresponds to the α-Si (starting material).

Sample No.	Thickness of α-Si or poly-Si	Laser energy (mJ/cm^2)	
		step 1	step 2
1	70	-	-
2	70	344	250
3	70	344	260
4	70	344	276

Variable angle-of-incidence spectroscopic ellipsometry has been measured in the wavelength range of 300 - 800 nm at an angle of incidence, 40°. The ellipsometric analysis was done by numerical inversion in three-layer model (air/SiO$_2$/α-Si or poly-Si/SiO$_2$/Si substrate). Numerical data of SiO$_2$ and Si, used for the analysis, are taken from ref. 7. The quantity used to describe an agreement between the experimental spectra and the

modeling process is given by the following expression:

$$\delta^2 = \frac{1}{N-p-1}\sum_{j=1}^{N}\left[\left(\tan\Psi_j^{\text{exp}} - \tan\Psi_j^{calc}\right)^2 + \left(\cos\Delta_j^{\text{exp}} - \cos\Delta_j^{calc}\right)^2\right] \qquad (4.1)$$

where N is the number of data points and p is the number of unknown model parameters. Here, "exp" and "calc" stand for measured and calculated values, respectively.

4.2.2 Results and discussion

The TEM micrographs and SE analyses show complete transition from amorphous-to-polycrystalline nature of Si films upon laser irradiation of energy 144 - 280 mJ/cm^2, but surface of samples become rough. Whereas, above 300 mJ/cm^2 of laser energy irradiated sample resulted amorphous but smooth. However, we found that, in two step irradiation process (i.e., an irradiation of above 300 mJ/cm^2 pulse followed by low energy pulse), a smooth crystalline Si can be obtained. Figure 4.1 shows the cross-sectional view of 250 mJ/cm^2 laser energy irradiated sample, where the surface is rough. The TEM cross-sectional view of two step irradiated sample (sample 2) is shown in Figure 4.1, for comparison. It is clear from Figs. 4.1(a) and 4.1(b) that, annealing in two step laser irradiation produces poly-Si with smooth surface. It is also evident from Fig. 4.1, that the sample 2 has an average grain size of 50 nm. Since samples irradiated in one step are not suitable for SE measurements due to their rough surface morphology, only samples those subjected to two step irradiation have been analyzed by SE.

It is known that the optical properties of amorphous materials are strongly dependent on growth condition. In order to obtain dielectric function of α-Si using SE measurements, the optical constants of α-Si was fitted by a Cauchy dispersion formula,

$$\begin{aligned} n &= A_0 + \frac{A_2}{\lambda^2} + \frac{A_4}{\lambda^4}, \\ k &= A_1 + \frac{A_3}{\lambda^3} + \frac{A_5}{\lambda^5} \end{aligned} \qquad (4.2)$$

where n represents the real part of the complex refractive index and k is the imaginary part of it.

Using the three-layer model, i.e. SiO_2/α-Si/SiO_2/substrate, it was possible to find an excellent fit for Ψ and Δ. The peak value of ε_2 is about 30, which is in agreement with
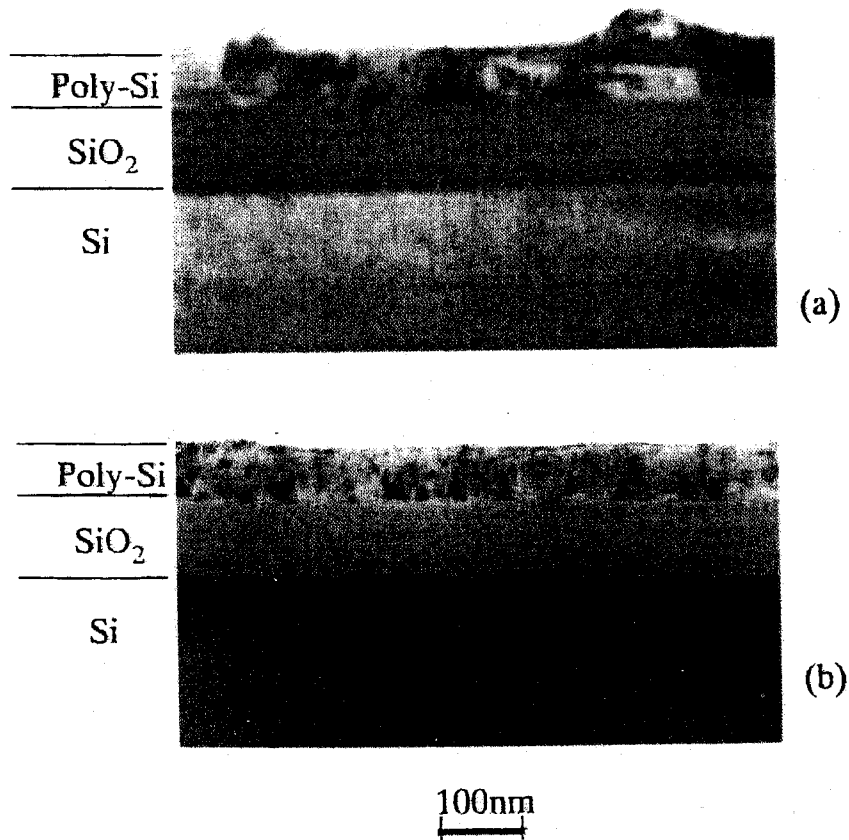
Figure 4.1: TEM cross-sectional micrographs of poly-Si thin films obtained by laser irradiation of α-Si. (a) 250 mJ/cm^2 laser energy irradiated sample, (b) sample 2 in Table 4.1.

those reported earlier obtained with high density α-Si.[8] This further indicates that our LPCVD-deposited α-Si film has high density.

It is assumed that the crystallized Si (poly-Si) films are physical mixture of α-Si and crystalline silicon (c-Si). The effective dielectric function of poly-Si films is represented by Bruggeman EMA[9]

$$0 = \sum_{i=1}^{n} f_i \frac{\varepsilon_i - \varepsilon}{\varepsilon_i + 2\varepsilon} \tag{4.3}$$

where ε_i and f_i ($\sum\limits_{i=1}^{n} f_i = 1$) are the dielectric function and the volume fraction, respectively, of the ith component. The best-fit three-layer model for sample 4 shown in Fig. 4.2, reveals that the EMA model provides a good fit to experimental SE data of Δ and Ψ. The parameters obtained by TEM and SE are summarized in Table 4.2.
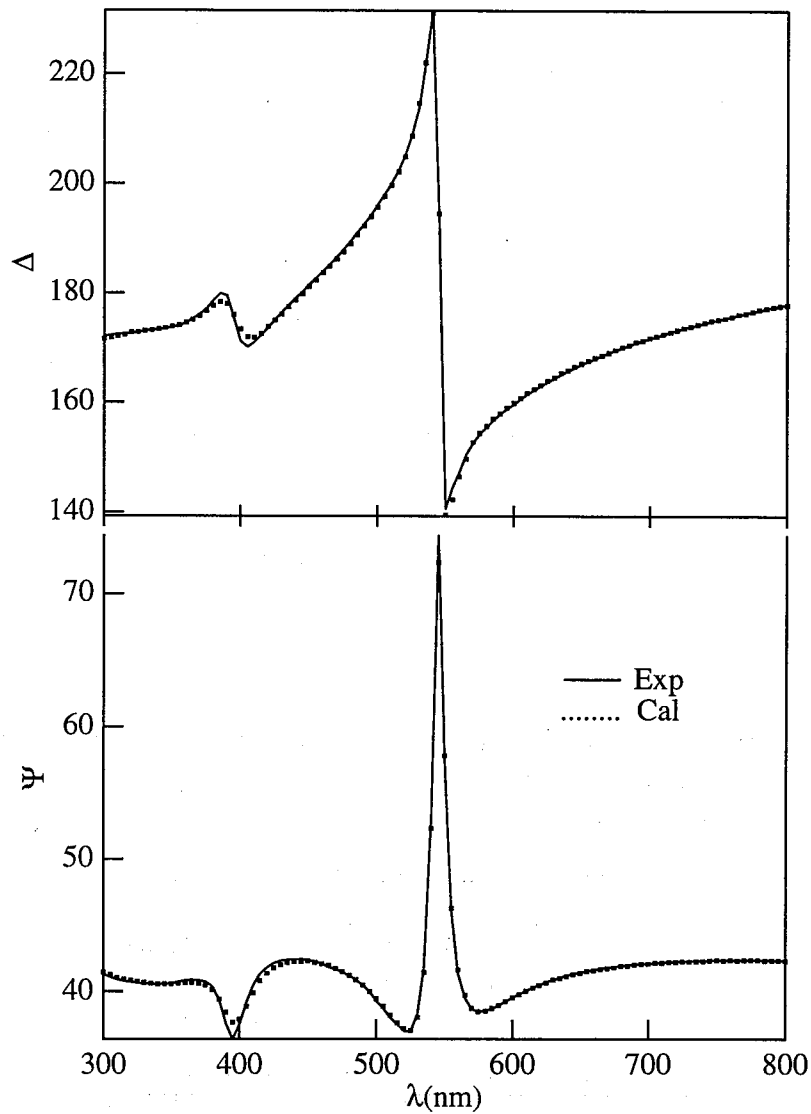

Figure 4.2: The spectra of both experimental (Broken lines) and calculated (according to EMA; Solid lines) data of Δ and Ψ for sample 4.

It is clear from Table 4.2 that the thickness of each layer obtained by SE are in agreement with that of TEM and the crystalline Si fraction increases from sample 2 to sample 4. On the other hand, the reduction of thickness of poly-Si films is attributed to the increase of

Table 4.2: EMA parameters of the best-fit three-layer model for poly-Si by laser irradiation.

Sample No.	Thickness (nm) of nature oxide film	Thickness (nm) α-Si or poly-Si		Thickness (nm) SiO$_2$		Volume fraction (%)		δ
		TEM	SE	TEM	SE	f_c	f_a	
1	3.68	68	70.30	100	100.0	-	-	0.003
2	3.54	68	69.10	100	100.0	86.2	13.8	0.073
3	2.01	-	68.31	-	100.0	86.8	13.2	0.03
4	2.21	-	66.58	-	100.0	91.3	8.7	0.045

film density. These results also correlate with the deduced dielectric functions given in Fig. 4.3. Plots for $\varepsilon(E)$ of α-Si and c-Si are also presented in Fig. 4.3, for comparison. One of the main features in the optical spectrum is the peak of $\varepsilon(E)$ at the interband transitions (E$_1$ critical point). The structure that appears in $\varepsilon(E)$ can be analyzed in term of standard analytic line shape.[10]

Table 4.3: The E$_1$ interband transition parameters (oscillator strength A, energy position E, broadening Γ, and phase angle ϕ) obtained by fitting the second derivative of the dielectric function spectra with 2D line shapes.

Sample No.	A	E(eV)	Γ	ψ
2	10.3	3.38	0.13	46.9
3	12.5	3.36	0.12	38.1
4	14.9	3.34	0.12	33.0
c-Si	19.5	3.38	0.076	51.4

$$\frac{d^2\varepsilon}{d\omega^2} = \begin{cases} n\,(n-1)\,Ae^{i\phi}\,(\omega - E + i\Gamma)^{n-2} & n \neq 0 \\ Ae^{i\phi}\,(\omega - E + i\Gamma)^{-2} & n = 0 \end{cases} \tag{4.4}$$

where A describes the amplitude, E the threshold energy of the CP, Γ its broadening, and ϕ a phase angle.

We fit simultaneously the real and imaginary parts of the numerically second-derivatives for the experimental $\varepsilon(\omega)$ by using the equation (4.4). The results of the E$_1$ structure
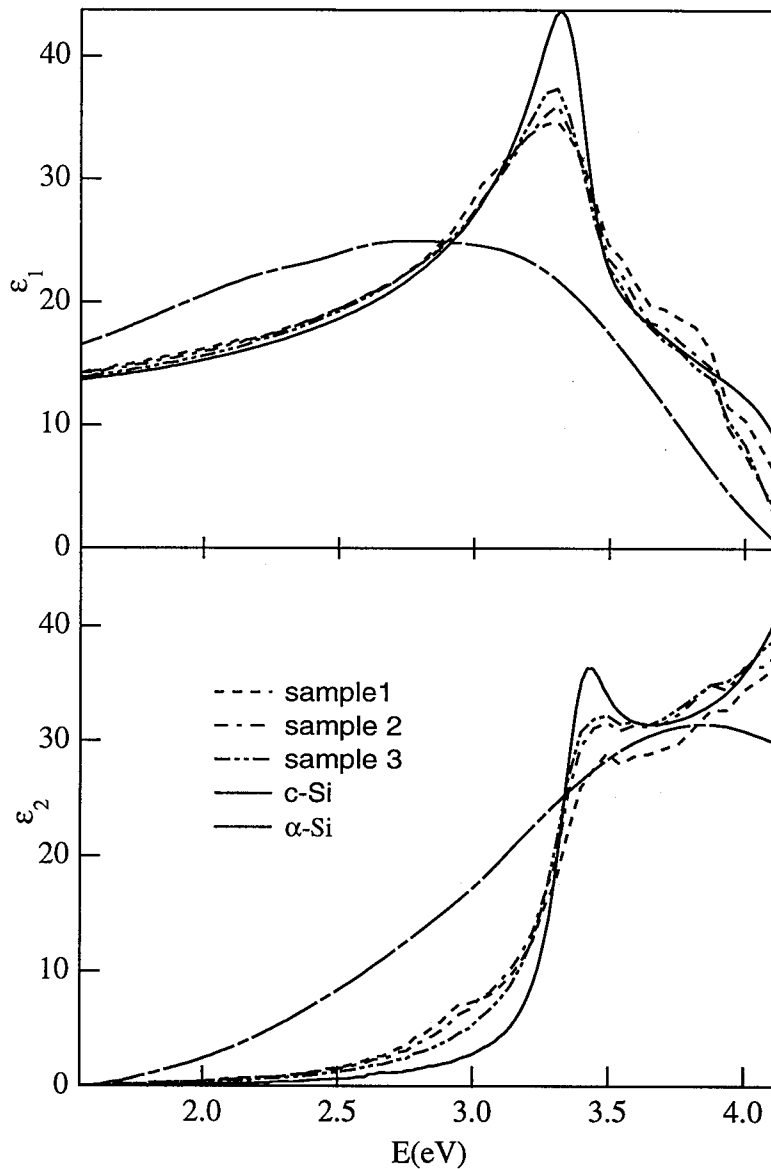
Figure 4.3: The spectra of dielectric function $\varepsilon(\omega)$ obtained from ellipsometric measurements for samples described in Table 4.1.

are given in Table 4.3. In the case of composite materials, the amplitudes of interband transitions are weighed by the percentage of crystalline component and crystalline grain size, while the broadening parameter is related to the reciprocal of the mean grain size.[11] Although, sample 4 has 91.3% crystalline fraction and 14.9 oscillator strength, the crystalline grain size is same as of sample 3. All three poly-Si films exhibit decrease of energy E_1 and is attributed to the poly-Si under tensile stress.[11]

4.3 Study on excimer laser annealed polycrystalline $Si_{1-x}Ge_x$ alloy thin films by X-ray diffraction and spectroscopic ellipsometry

4.3.1 Experimental

A germanium target, partly covered with silicon wafers, has been used for the deposition of $Si_{1-x}Ge_x$ /Si alloy thin films, of different compositions (x), by Ar^+ ion beam sputtering. Single crystal Si (100), 2° off towards [011], and glass are used as substrates. The arbitrary composition can simply be controlled by varying the area of Si wafers. The deposition has been carried at a base pressure of 2×10^{-6} torr, and at room temperature, using the beam voltage of 1 kV, beam current of 20 mA and power of 20 W. These films have been analyzed by various analytical techniques and the results are discussed in the following sections.

The resulting films are smooth with excellent adhesion to the substrate. Crystallization was carried at room temperature and in air using a XeCl excimer laser ($\lambda = 308$ nm) which provides an area of 5 mm × 5 mm and pulses of 20 ns (FWHM) duration. Samples were annealed by the irradiation of one laser pulse, and different laser pulse energies of 92 to 212 mJ/cm² were used. Details concerning the laser irradiation conditions for various samples studied are listed in Table 4.4.

The structural characterization and grain size determination of the films are performed using an X-ray diffractometer with CuK_α radiation. All the patterns are recorded at an angular speed as low as 0.2°/min by steps of 0.02° and with a voltage of 40 kV and current of 35 mA in the standard $\theta - 2\theta$ geometry. The crystallographic preferred orientation of polycrystalline films is measured by comparing the intensity of the different diffraction peaks with a randomly oriented polycrystalline film, and the integral linewidth and Bragg angle are determined by fitting directly the diffraction profile using the convolution equation between the pure profile and the Deby-Scherrer instrumental profile, and are discussed in detail in the following X-ray section. The optical transmission in the wavelength range (between 400 nm to 1600 nm) was measured using a UV-visible spectrophotometer. The composition and formation of $Si_{1-x}Ge_x$ /Si alloys have been realized from surface and depth

Table 4.4: Experimetal details of ion beam sputtered poly-$Si_{1-x}Ge_x$ /Si alloy thin films.

Sample no.	Substrate	Composition (x)	Energy of laser irradiation (mJ/cm^2)
1	Glass	0.23±0.01	212
2	Glass	0.23±0.01	164
3	Si	0.23±0.01	212
4	Si	0.23±0.01	164
5	Glass	0.36±0.01	212
6	Glass	0.36±0.01	164
7	Si	0.36±0.01	212
8	Si	0.36±0.01	164

profile analyses using the auger electron spectroscopy.

Since the CP energy strongly depends on the composition of $Si_{1-x}Ge_x$ /Si alloys and also may be shifted due to the oxidation/roughening,[24] it is necessary to treat the surface before SE measurements in order to estimate the composition of poly-$Si_{1-x}Ge_x$ /Si. Therefore, we have polished our samples with Syton-saturated lens paper, followed by rinse with water. This process was repeated until the largest value of ε_2 at E_2 (about 4.3 eV) was obtained. Optical data were recorded with a polarizer-sample-rotating-analyzer spectroellipsometer, at room temperature. Variable angle-of-incidence spectroscopic ellipsometry has been measured, for samples sputtered on both the glass and Si substrates, in the wavelength range of 260 - 830 nm with a step of 5 nm at an angle of incidence 60°. During the measurement the surface treated samples were maintained in a drying N_2 flow to eliminate various surface contamination effects. All the SE plots presented in this paper are for samples deposited on glass substrate. However, the data obtained from SE measurement of samples deposited on Si substrate are tabulated and discussed in respective following sections.

4.3.2 Results and discussion

X-ray diffraction

Figure 4.4 shows the X-ray diffraction patterns on samples of as-deposited [pattern (a)] and laser annealed [patterns (b), (c), (d), and (e) respectively for samples 1, 3, 5, and 7] structures of two different $Si_{1-x}Ge_x$ /Si compositions, x = 0.23 [(b) and (c)] and x = 0.36 [(d) and (e), these compositions are derived from SE measurements and are discussed in the following section, deposited on Si [(a), (c) and (e)] and glass [(b) and (d)] substrates by ion beam sputtering. In the as-deposited case, with both the substrates, we observe the amorphous nature of the thin film with two halos [Fig. 4.4(a), on Si substrate]. The first, centered at $2\theta = 28°$ close to the position of the (111) crystalline diffraction peak corresponds to the existence of short-range diamond cubic structure. And the other, located at covering $2\theta = 45$ - $55°$ may be due to the (220) and the (311) crystalline peaks. For laser annealed samples, the three peaks corresponding to (111), (220), and (311) indicate the polycrystalline nature of the films upon laser irradiation.

To determine the grain size of the samples it is necessary to correct lines for the experimental aberrations. In order to obtain the Deby-Scherrer instrumental profile $g(\theta)$, we measured larger-grain-size polycrystalline silicon powder,[26] and the experimental profile is very well fitted with the function.[27]

$$f(x) = C/\left[1 + (x/k)^2\right]^2.$$

(4.5)

In the above expression, C and k are adjustable constants and x is the abscissa measured from the profile maximum. An experimental profile $h(\theta)$, that is directly observable, is the convolute between a weight function $g(\theta)$ and a pure diffraction profile $f(\theta)$,[28]

$$h(\varepsilon) = \int_{-\infty}^{\infty} g(\zeta) f(\varepsilon - \zeta) d\zeta.$$

(4.6)

A pure diffraction profile free of instrumental contributions $f(\varepsilon)$ in Eq. 4.6, is also assumed as Eq. 4.5. Experimental profiles of the $Si_{1-x}Ge_x$ /Si alloys of two different compositions (Fig. 4.4) are well fitted using the Eq. 4.6 as shown in Figure 4.4 by solid lines. And, the
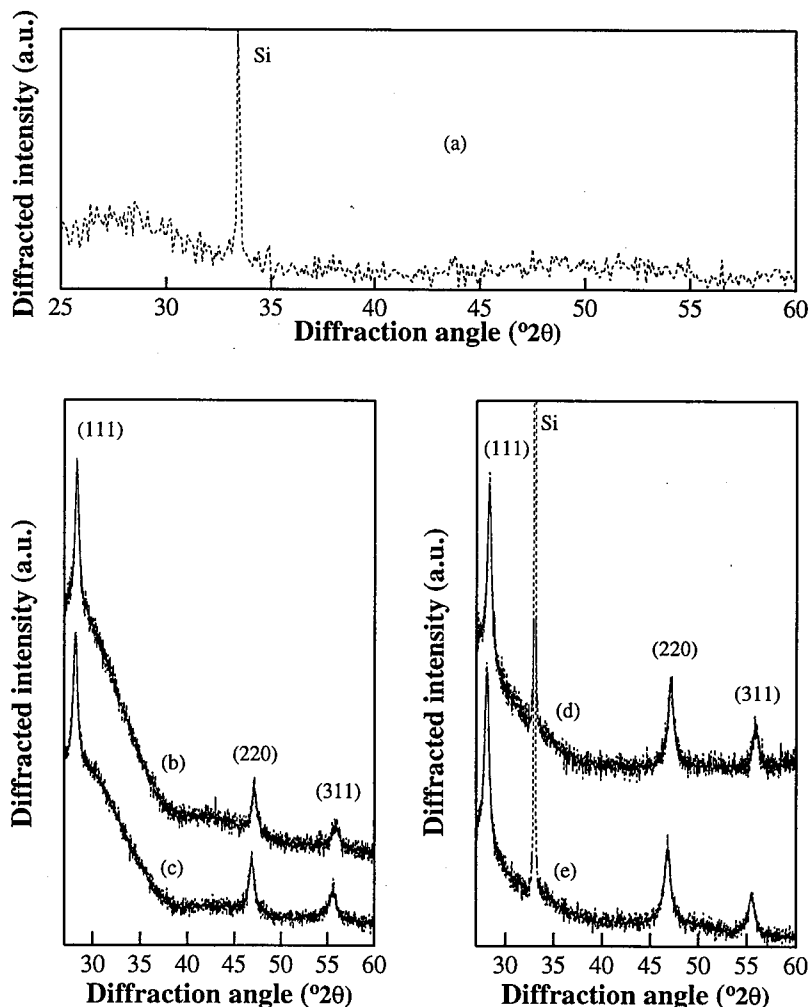
Figure 4.4: X-ray diffraction patterns of ion beam sputtered $Si_{1-x}Ge_x$ /Si alloy thin films of as-deposited [(a)] and laser irradiated [(b)-(e)] samples of two different compositions, x = 0.23 [(b) and (c)] and x = 0.36 [(d) and (e)], deposited on Si [(a), (c) and (e)] and glass [(b) and (d)] substrates. (a) as-deposited, (b) sample 1, (c) sample 3, (d) sample 5, and (e) sample 7. Experimental curves are very well fitted (solid line) with the function mentioned as Eq. 2 in the text.) data of Δ and Ψ for sample 4.

integral linewidth has been determined for these line profiles in order to evaluate the grain size l, using the classical Scherrer equation,

$$l = k_s \lambda / \Delta \cos \theta \qquad (4.7)$$

where θ is the Bragg angle, *lambda* the wavelength of the radiation used, k_s a constant[26] close to 1.05 and Δ is the integral linewidth. In order to determine the crystallographic preferred orientation of growth, we calculated the normalized intensity ratio of each sample

(i) α_i and β_i defined by

$$\alpha_i = I_{i(220)} \big/ I_{p(220)},$$

$$\beta_i = I'_{i(311)} \big/ I'_{p(311)},$$

where $I_i = C_{i(220)}/C_{i(111)}$ and $I'_i = C_{i(311)}/C_{i(111)}$ are the intensity ratios of the pure diffraction profiles determined by fitting, and I_p and I'_p are the fractions measured from the intensities of the Bragg peaks for the standard randomly oriented silicon powder infinitely thick, which takes into the account of the absorption coefficient of the film for the radiation used.[26] The results are listed in Table 4.5. These results indicate that the (111) orientation is dominant in the samples deposited on both glass and Si substrates, together with the orientation dominance of (311) peak in the case of samples deposited on Si substrate: this is associated with the difference of free surface energy between the Si and glass substrates. Under the excimer laser irradiation, it is reported that the recrystallization starts from the surface of amorphous Si deposited over the glass substrate and the (111) orientation was dominant.[29] Therefore, the free surface energy of a film also play an important role, same as the case of UHV annealed amorphous Si on quartz.[30] On the other hand, the Si substrate could act as a seed for crystal growth for the excimer laser annealing process.[31] Since the Si (100) 2° off towards [011] were used as substrate in our experiments, the surface of Si substrate are composed of deformed steps of molecular dimensions, thus the simultaneous dominance of 311 planes is not surprising.[26] Also, from Table 4.5, it is clear that the grain size decreases with increasing Ge mole fraction irrespective of the substrate used (either Si or glass) and this may be explained as follows. Y. Morita et al.[32] had reported that the grain size increases with the increasing energy of laser irradiation for amorphous Si on glass. Furthermore, our SE measurements show that the absorption spectrum shifts towards longer wavelengths and the absorption coefficient decreases with increasing Ge mole fraction for amorphous Si$_{1-x}$Ge$_x$ /Si films at the wavelength of excimer laser (308 nm). Combining the two observations of Morita et al and our SE measurements, we can say that under the same energy of laser irradiation, different amounts of laser energy was absorbed by the deposited films due to the variation in the composition, which alters

the degree of annealing and hence the change in the degree of crystallinity.

Table 4.5:

Sample No.	<111>			<220>			<311>			α	β
	2θ (degree)	k	grain size (nm)	2θ (degree)	k	grain size (nm)	2θ (degree)	k	grain size (nm)		
1	28.262 ±0.005	0.342 ± 0.01	86.2	47.047 ±0.01	0.496 ± 0.03	36.4	55.769 ±0.02	0.688 ± 0.06	22.4	0.61	0.64
3	28.274 ±0.005	0.333 ± 0.02	88.4	47.025 ±0.01	0.323 ± 0.04	55.9	55.785 ±0.02	0.521 ± 0.04	29.5	0.68	0.94
5	28.097 ±0.005	0.383 ± 0.01	77.4	46.768 ±0.008	0.511 ± 0.02	34.8	55.460 ±0.02	0.654 ± 0.04	23.7	0.76	0.80
7	28.090 ±0.004	0.377 ± 0.01	78.6	46.754 ±0.01	0.433 ± 0.04	41.1	55.456 ±0.01	0.630 ± 0.03	24.6	0.66	0.93

Table 4.5. X-ray diffraction results of poly-$Si_{1-x}Ge_x$ alloy thin films.

The lattice parameters of $Si_{1-x}Ge_x$ /Si alloys of the two different compositions are found to be 0.5465 nm and 0.5496 nm, respectively. It is observed that the lattice parameter

increases with increasing Ge concentration. The difference in composition between the samples of two different Ge concentrations can be estimated from the plot of lattice constant versus Ge mole fraction, assuming a linear relation between the lattice constants of Si (0.543095 nm) and Ge (0.564613 nm).[33] And is found to be 0.144, which is in agreement with the value (0.13) obtained by SE. However, we cannot rule out the effect of strain present in our samples. An analysis of strain has been discussed together with the ellipsometric results in the following section.

Spectroscopic ellipsometry

The pseudodielectric function is given by

$$\langle \varepsilon \rangle = \langle \varepsilon_1 \rangle + i \langle \varepsilon_2 \rangle = \sin^2 \phi \left\{ 1 + [(1 - \rho)/(1 + \rho)]^2 \tan^2 \phi \right\}, \tag{4.8}$$

where ϕ is the angle of incidence. ε is a quantity derived from the SE data using the two-phase (ambient/substrate) model, and therefore corresponds to samples where there is no overlayer. The pseudodielectric function spectra (ε_1 and ε_2) of as-deposited, laser irradiated and Syton polished $Si_{1-x}Ge_x$ /Si alloys of two different compositions x = 0.23 and 0.36 (samples 1 and 5) are shown in Figs. 4.5 and 4.6 respectively. In the same Figs. 4.5 and 4.6, the dielectric function of $Si_{1-x}Ge_x$ /Si alloys of the two compositions (x = 0.23 and 0.36) obtained from the interpolation procedure[21] and that of poly-Si[34] were also plotted for comparison. It is clear from these figures that the as-deposited films are amorphous and convert to poly-$Si_{1-x}Ge_x$ /Si after excimer laser irradiation. The analysis of pseudodielectric function spectra of laser irradiated samples, using a four phase (ambient/SiO2/rough layer/poly-$Si_{1-x}Ge_x$ /Si) model, has demonstrated that the samples consist of about 6.8 nm overlayer on the surface. Further, the Syton polished samples have larger values of ε_2 at E_2 (about 4.3 eV) compared with that of laser irradiated (un polished) surface (Figs. 4.5 and 4.6). Therefore, these samples are assumed having close to ideal surface quality, and further analysis was done only on Syton polished samples by both SE and transmission measurements.

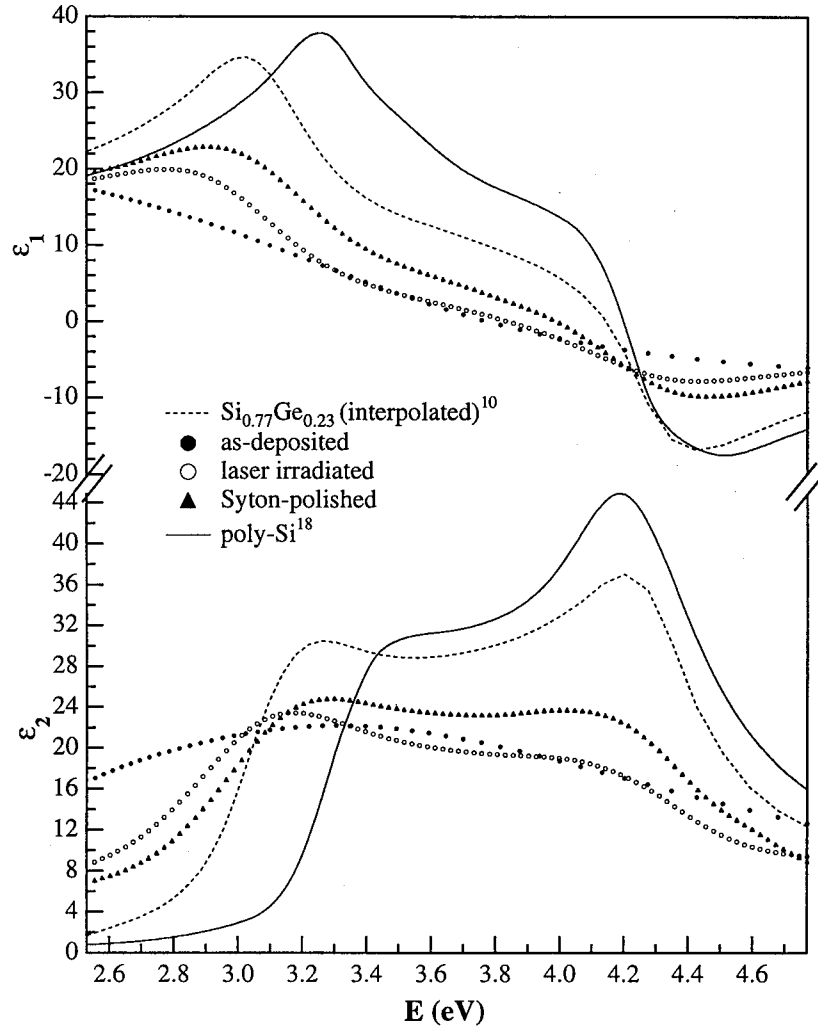The structure in the vicinity of the so-called critical-points (CPs) that appear in $\varepsilon(\omega)$

Figure 4.5: The pseudodielectric function spectra ($\varepsilon = \varepsilon_1 + i\varepsilon_2$) of as-deposited, laser irradiated (sample 1) and Syton polished surface of sample1. The dielectric function spectra of poly-Si and the interpolated spectrum of $Si_{0.77}Ge_{0.23}$ are also shown for comparison.

can be analyzed in terms of standard analytic line shapes. The two-dimensional CP and the $\varepsilon(\omega)$ can be expressed as:

$$\varepsilon(\omega) \approx A \ln(E_g - \omega + i\Gamma) e^{i\phi}, \tag{4.9}$$

where A describes the amplitude, E_g the threshold energy of the CP, Γ its broadening, and ϕ the phase angle.

The experimental second derivative (obtained by numerical differentiation of the original spectra) can enhance the structure in the spectra and the line-shape analysis of the CP can be performed using a least-squares in order to determine the parameters E_g, A, Γ, and ϕ. In
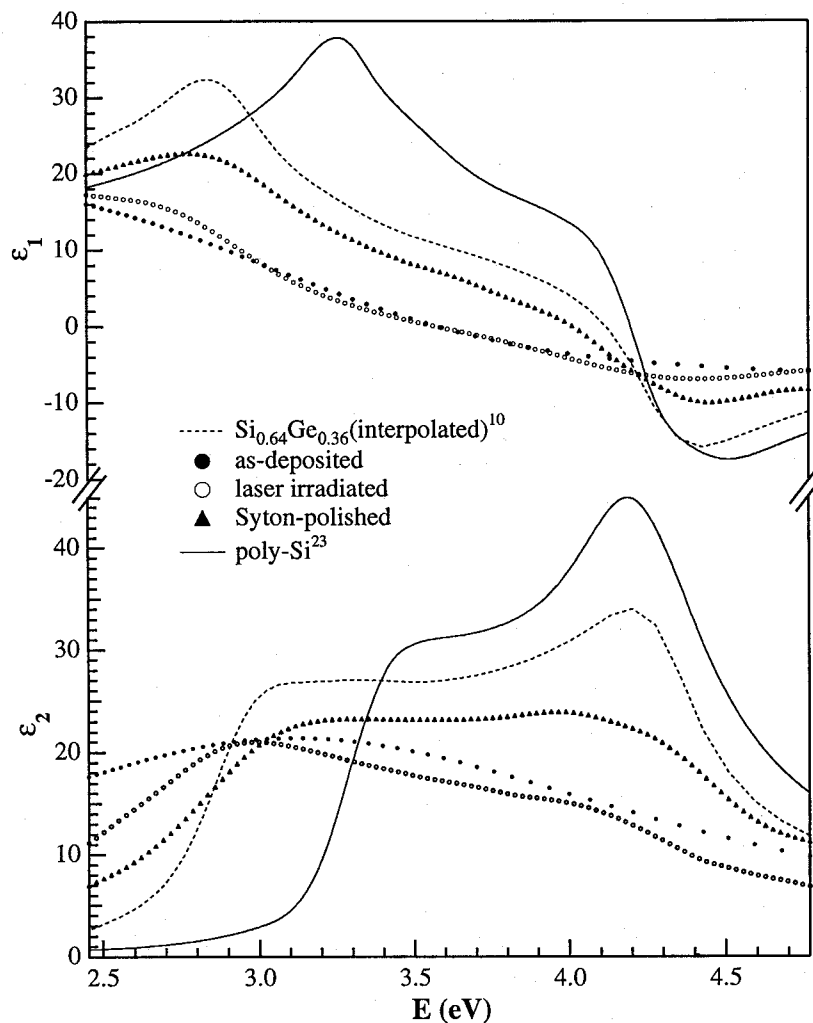
Figure 4.6: The pseudodielectric function spectra $(\varepsilon = \varepsilon_1 + i\varepsilon_2)$ of as-deposited, laser irradiated (sample 5) and Syton polished surface of sample 5. The dielectric function spectra of poly-Si and the interpolated spectrum of $Si_{0.64}Ge_{0.36}$ are also shown for comparison.

Fig. 4.7, the second derivative spectrum of our laser irradiated poly-$Si_{1-x}Ge_x$ /Si alloys for two different compositions, x = 0.23 (b) and x = 0.36 (c) are shown and compared with that of poly-Si (a).[34] The structures from our poly-$Si_{1-x}Ge_x$ /Si, attributed to E_1 $(L_3^v \rightarrow L_3^c)$ and E_2 $(X_4^y \rightarrow X_1^c)$ transitions, can be clearly seen from Fig. 4.7, and it is evident that the peak of E_1 shifts toward lower energy compared to the poly-Si. The results of the second-derivative analysis of the E_1 structure assuming one CP are given in Table 4.6. It is reported that the $Si_{1-x}Ge_x$ /Si films on Si substrate are under compressive stress,[24] and the thicker (above 40 nm) poly-Si films on SiO_2 exhibit internal tensile stress.[35] However, it is clear from Table 4.6 that the values of E_1 have no obvious difference, irrespective of
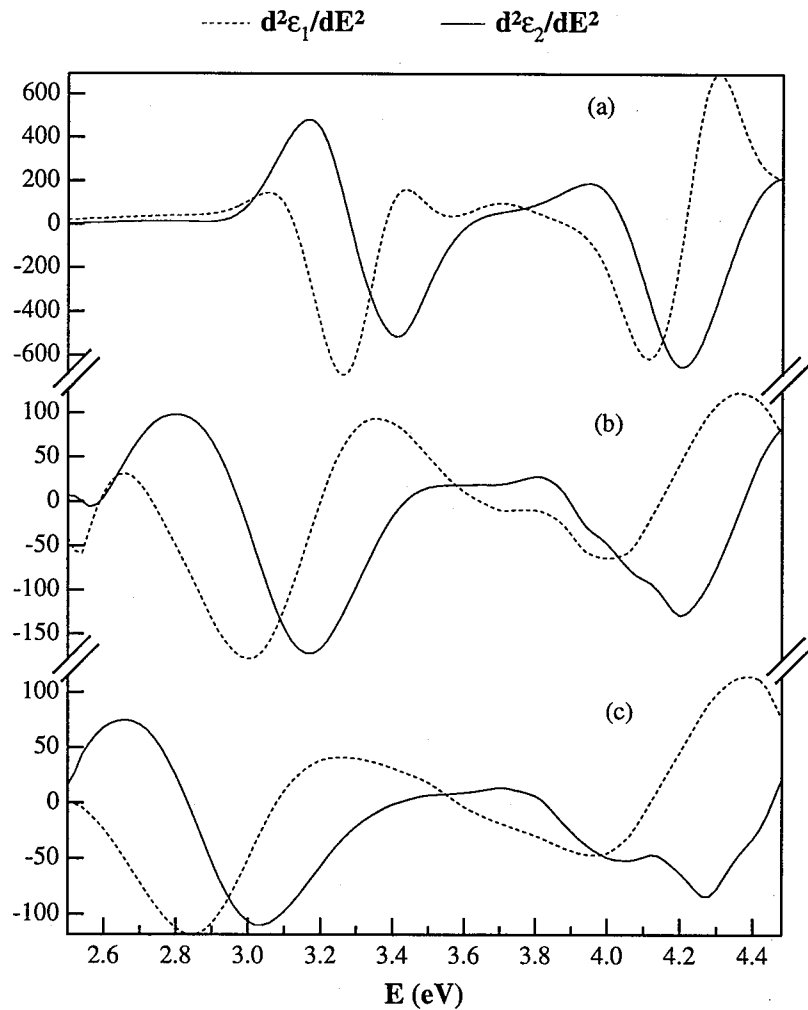
Figure 4.7: The numerically differentiated second derivative spectra of ($\varepsilon = \varepsilon_1 + i\varepsilon_2$) for, (a) poly-Si23, and our Syton polished samples, (b) sample 1 and (c) sample 5.

the substrate used (either Si or glass), for a particular composition. Hence, we estimate all our films are relaxed from the strain in the near surface because the penetration depth of the light beam is about 10 nm at around E_1 peak wavelength. Therefore, the shift in the E_1 peak energies between the poly-$Si_{1-x}Ge_x$ /Si [Figs. 4.7 (b) and (c)] and poly-Si [Fig. 4.7 (a)] is mainly attributed to the Ge mole fraction. Furthermore, the shift between the two different compositions [Figs. 4.7 (b) and (c)] indicate the difference in the concentration of Ge in poly-$Si_{1-x}Ge_x$ /Si alloys. The mole fraction of Ge has been evaluated according to the relation between the composition (x) and E_1 developed by Humlicek et al. and found to be about 0.23 ± 0.01 and 0.36 ± 0.01 for two different compositions. These results are

Table 4.6: The E_1 interband transition parameters (amplitude A, threshold energy E_g, broadening Γ, and phase angle ϕ) obtained by fitting the second derivative of the dieletric function spectra of poly-$Si_{1-x}Ge_x$ /Si alloy thin films.

Sample no.	A	E_g (eV)	Γ (meV)	$\phi(°)$
1	54.8	3.086	147	-0.76
2	49.4	3.076	157	-1.64
3	52.8	3.088	163	-0.303
4	48.1	3.078	169	-16.08
5	47.1	2.895	175	-20.39
6	43.7	2.877	190	-8.96
7	40.8	2.905	169	-10.97
8	40.8	2.903	185	-13.97

in agreement with X-ray and AES measurements which reveal the formation of $Si_{1-x}Ge_x$ /Si alloys of two different compositions. Using these compositions, once again according to the linear relationship mentioned in X-ray section, the lattice constants of $Si_{1-x}Ge_x$ /Si alloys of two different compositions x = 0.23 and 0.36 are found to be 0.5480 nm and 0.5508 nm, respectively. These values are slightly larger than those obtained by X-ray analyses (0.5465 nm and 0.5496 nm), may be due to the influence of microstrain which is neglected for SE measurements as mentioned above. However, the slight difference in lattice parameters obtained from the two different techniques, for the same composition, may be related to the presence of strain. Hence, it is clear from these results that the shift in diffraction peaks for the two different compositions is not only due to the difference in Ge concentration but also due to the compressive strain as is evidenced from the difference in lattice parameters obtained from XRD and SE measurements. The magnitude of the strain was estimated to be -0.003, which is almost more than half of that of single crystalline $Si_{0.78}Ge_{0.22}$ grown on Si substrate.[24] However, this strain does not change the results of grain size as it is uniform compressive strain.[36] The values of broadening (Γ) has been interpreted in terms of the mean grain size of the poly-$Si_{1-x}Ge_x$ /Si alloys and similar conclusions have been derived earlier in case of poly-Si thin films.[35] However, no matter

what substrates are used, in a particular composition, the broadening decreases (i.e., grain size increases) with increasing energy of laser irradiation. In order to obtain quantitative

Table 4.7: The best fit parameters determined by SE measurements. The 90% confidence limits are given with ($\pm$). Also, the optical gap E$_{04}$, the energy at which the absorption coefficient α is 10^4 cm^{-1}, measured by uv-visible spectroscopy is presented.

| Sample | Composition | | | | Thickness | | E$_{04}$ |
no.		c-Si$_{1-x}$Ge$_x$	α-SiGe	Void	(nm)	δ	(eV)
1		0.692± 0.02	0.222± 0.02	0.086	257.0± 2.1	0.045	1.28
2	x=0.23	0.578± 0.02	0.335± 0.02	0.087	260.8± 2.6	0.048	1.19
3	±0.01	0.602± 0.03	0.332± 0.03	0.066	263.1± 5.7	0.035	-
4		0.494± 0.02	0.431± 0.03	0.075	253.4± 5.0	0.027	-
5		0.728± 0.02	0.209± 0.02	0.063	271.3± 2.4	0.038	1.15
6	x=0.36	0.588± 0.02	0.316± 0.02	0.096	283.2± 3.0	0.038	1.05
7	±0.01	0.591± 0.03	0.349± 0.04	0.060	275.9± 8.8	0.045	-
8		0.488± 0.03	0.461± 0.03	0.051	285.4± 9.0	0.039	-

information through the analysis of the SE measurements (Δ, Ψ), we have calculated the dielectric function of poly-Si$_{1-x}$Ge$_x$ /Si of composition x=0.23 and x=0.36 according to the interpolation procedure developed by Snyder et al.. We analyzed SE data of the Syton-polished poly-Si$_{1-x}$Ge$_x$ /Si surface using a three-phase (ambient/poly-Si$_{1-x}$Ge$_x$ /Si/Si or glass substrate) model. The poly-Si$_{1-x}$Ge$_x$ /Si is assumed as a composite material consisting of crystalline Si$_{1-x}$Ge$_x$ /Si, amorphous Si$_{1-x}$Ge$_x$ /Si and void. The dielectric response of these films were represented by the Bruggeman effective-medium theory (EMT). The mathematical formula can be expressed as:

$$\sum_{i=1}^{n} f_i \frac{\varepsilon_i - \varepsilon}{\varepsilon_i + 2\varepsilon} = 0, \tag{4.10}$$

where ε_i and f_i $(\sum f_i = 1)$ are the dielectric function and volume fraction, respectively, of the ith component. The unknown parameters can be numerically determined by minimizing the following meansquares deviation with a regression program (unbiased):[35]

$$\delta^2 = \frac{1}{N-P-1}\left(\sum_{i=1}^{N}\left|\rho_i^{\exp t} - \rho_i^{calc}\right|^2\right), \tag{4.11}$$

where N is the number of data points and P is the number of unknown model parameters. All the parameters derived from this analysis are summarized in Table 4.7. It is to be noted that our poly-$Si_{1-x}Ge_x$ /Si alloy thin films has the density deficit because the void fraction is positive. However, this deficit is larger in films deposited on glass over to that of Si. Moreover, it is obvious from these results that the density and the volume fraction of crystalline $Si_{1-x}Ge_x$ /Si increases with increasing energy of laser irradiation. Also, it is to be noted that the volume fraction of crystalline $Si_{1-x}Ge_x$ /Si of films deposited on glass substrate is slightly larger than that of films on Si substrate, irrespective of the composition x. This may be due to the time of recrystallization on Si substrate is shorter than that on glass substrate because, the thermal conductivity of Si is larger than glass.

UV-Visible Absorption Spectroscopy

Fig. 4.8 shows the spectrum of absorption coefficient versus photon energy for Syton polished samples 1 and 5 from the uv-visible transmission measurements. Since the Tauc's gap is not valid for microcrystalline or biphasic materials,[37] the optical gap of our $Si_{1-x}Ge_x$ /Si alloys of two different compositions are evaluated in terms of E_{04}, the energy at which the absorption coefficient (α) is 10^4 cm^{-1}.[38,39] These values are listed in Table 4.7. It is clear from Tables 4.4 and 4.7 that the E_{04} decreases with increasing Ge mole fraction and decreasing the energy of laser irradiation. These results further support the conclusions derived from the X-ray and SE, that the degree of crystallinity depends on the energy of laser irradiation and amount of Ge concentration, the two key factors which determine the value of E_{04}.
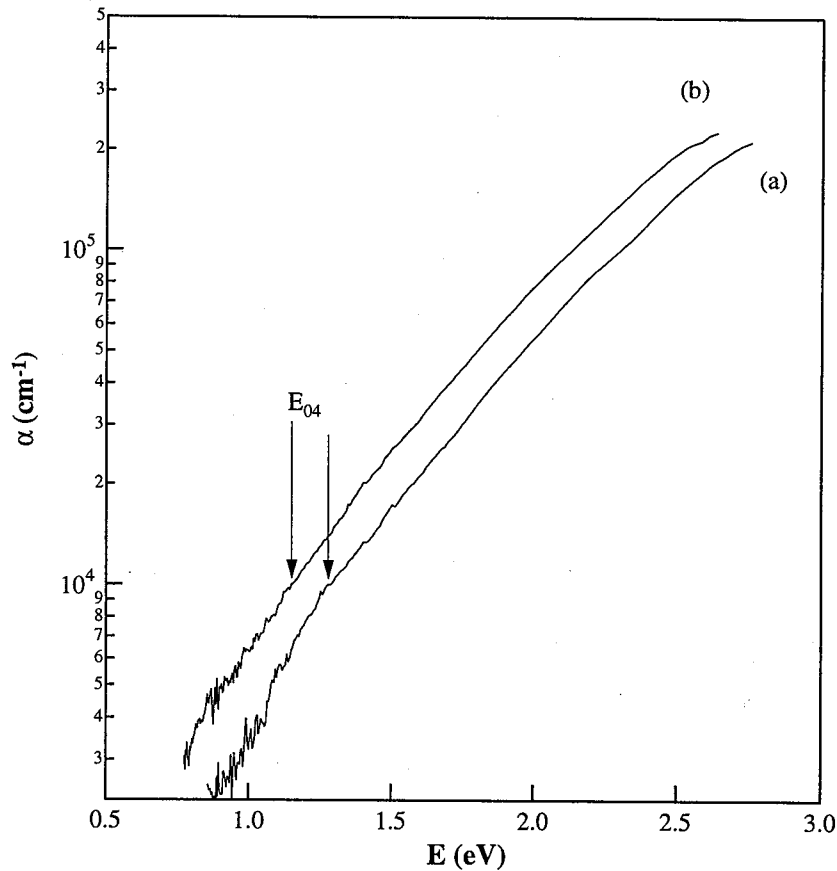
Figure 4.8: Plots of absorption coefficient α versus photon energy E, for Syton polished surface of samples 1 and 5 [(a) and (b), respectively], in order to obtain the optical gap of the films in terms of E_{04} (defined as the energy at which α is equal to 10^4 cm^{-1}).

4.4 Conclusions

Poly-Si thin films, obtained by the crystallization of α-Si by laser annealing have been studied. Smooth poly-Si films have been obtained by the implementation of two step irradiation technique, i.e., 344 mJ/cm^2 pulse followed by 250 - 276 mJ/cm^2 laser energy pulse. A detailed analysis of the $\varepsilon(\omega)$ demonstrate that increase of laser energy lead to an increase of the crystalline fraction and the crystalline grain size. It has also been observed that the crystalline size saturates at 260 mJ/cm^2 laser energy. Also, poly-Si films exhibit tensile stress.

An amorphous thin films of $Si_{1-x}Ge_x$ /Si alloys have been deposited on glass and single crystal Si substrates by ion beam sputtering, and the composition (x) is controlled by varying the area of silicon wafers placed on the germanium target. Upon XeCl excimer laser

annealing, these films reveal polycrystalline nature by both X-ray and SE measurements. The composition (x) of $Si_{1-x}Ge_x$ /Si films, evaluated from the SE dielectric function $\varepsilon(\omega)$ data using the second derivative technique, are in agreement with those obtained from X-ray and AES measurements within their experimental limitations.

It has also been observed that the (111) orientation is predominant in all of poly-$Si_{1-x}Ge_x$ /Si films on both the substrates. This dominant of (111) orientation is attributed to the free surface energy of films which plays a major role in the crystallization process. Furthermore, the detailed analysis of X-ray diffraction data and SE measurements show that the average microcrystallite size decreases with increasing Ge mole fraction, and the volume fraction of crystalline $Si_{1-x}Ge_x$ /Si increases with increasing laser irradiation energy. These phenomena have been attributed to different degree of annealing and hence the changing in the degree of crystallinity.

Finally, the optical gap of these films have been obtained in terms of E_{04} (defined as the energy at which α is equal to 10^4 cm^{-1}) from the absorption coefficient spectra and the value is found to be in the range of 1.05 - 1.28 eV for two Ge concentrations. These results further support to conclude that the $Si_{1-x}Ge_x$ /Si alloy provides continuously and widely variable optical band gap.

References

[1] P. Mei, J. B. Boyce, M. Hack, R. Lujan, S. E. Ready, D. K. Fork, R. I. Johnson and G. B. Anderson, J. Appl. Phys., **76**, 3194 (1994).

[2] K. Yamamoto, A. Nakashima, T. Suzuki, M. Yoshimi, H. Nishio and M. Izumina, Jpn. J. Appl. Phys. **33**, L1751 (1994).

[3] F. Plais, P. Legagneux, C. Reita, O. Huet, F. Petinot, D. Pribat, B. Godard, M. Stehle and E. Fogarassy, Microelectronic Engineering **28**, 443 (1995) .

[4] T. Serikawa, S. Shirai, A. Okamoto and S. Suyama, Jpn. J. Appl. Phys. **28**, L1871 (1989).

[5] M. Fang and B. Drevillon, J. Appl. Phys. **71**, 5445 (1992).

[6] T. Suzuki and S. Adachi, Jpn. J. Appl. Phys: **32**, 4900 (1993).

[7] H. R. Philipp: Handbook of Optical Constants Solids, ed. E. D. Palik (Academic, Orlando, 1985).

[8] D. E. Aspnes, A. A. Studna and E. Kinsbron, Phys. Rev. **29**, 768 (1984).

[9] M. Erman, J. B. Theeten, P. Chambon, S. M. Kelso and D. E. Aspnes, J. Appl. Phys. **56**, 2664 (1984).

[10] P. Lautenschlager, M. Garriga, L. Vina and M. Cardona, Phys. Rev. **36**, 4821 (1987).

[11] S. Boultadakis, S. Logothetidis and S. Ves, J. Appl. Phys. **72**, 3648 (1992).

[12] S. Lombardo, A. Pinto, V. Raineri, P. Ward, G. La Rosa, G. Privitera, and S. U. Campisano, IEEE Electron Device Lett. **17**, 485 (1996).

[13] A. Slaoui, C. Deng, S. Talwar, J. K. Kramer, and T. W. Sigmon, Appl. Phys. A **59**, 203 (1994).

[14] I. Manna, Le-Tien Jung, and S. Banerjee, IEEE Proc. of 53rd Annual Device Res. Conf. Digest (1995) p. 156.

[15] E. A. Al-Nuaimy and J. M. Marshall, Appl. Phys. Lett. 69, 3857 (1996).

[16] A. Slaoui, C. Deng, S. Talwar, J. K. Kramer, B. Prevot, and T. W. Sigmon, MRS Symp. Proc. **321**, 689 (1994).

[17] A. Slaoui, C. Deng, S. Talwar, J. K. Kramer, T. W. Sigmon, J. P. Stoquert, and B. Prevot, Appl. Surf. Sci. **86**, 346 (1995).

[18] X. Zhang, Z. Chen, D. Cui, G. Yang, and R. Wang, Appl. Phys. Lett. **69**, 3164 (1996).

[19] D. Labrie, G. C. Aers, H. Lafontaine, R. L. Williams, S. Charbonneau, R. D. Goldberg, and I. V. Mitchell, Appl. Phys. Lett. **69**, 3866 (1996).

[20] S. F. Nelson and T. N. Jackson, Appl. Phys. Lett. **69**, 3563 (1996).

[21] J. Humlicek, M. Garriga, M. I. Alonso, and M. Cardona, J. Appl. Phys. **65**, 2827 (1989).

[22] N. V. Nguyen, K. Vedam, and J. Narayan, J. Appl. Phys. **67**, 599 (1990).

[23] R. T. Carline, C. Pickering, D. J. Robbins, W. Y. Leong, A. D. Pitt, and A. G. Cullis, Appl. Phys. Lett. **64**, 1114 (1994).

[24] C. Pickering, R. T. Carline, D. J. Robbins, W. Y. Leong, S. J. Barnett, A. D. Pitt, and A. G. Cullis, J. Appl. Phys. **73**, 239 (1993).

[25] P. G. Snyder, J. A. Woolam, S. A. Alterovitz, and B. Johs, J. Appl. Phys. **68**, 5925 (1990).

[26] R. Bisaro, J. Magarino, N. Proust, and K. Zellama, J. Appl. Phys. **59**, 1167 (1986).

[27] F. R. L. Schoening, J. Van Niekerk, and R. A. W. Haul, Proc. Phys. Soc. London **65B**, 528 (1952).

[28] H. P. Klug and L. E. Alexander, X-ray Diffraction Procedures for Poly-crystalline and Amorphous Materials (Wiley, New York, 1954), Chap.9, p. 491.

[29] E. L. Mathe', J. G. Maillou, A. Naudon, E. Fogarassy, M. Elliq, and S. De Unamuno, Appl. Surf. Sci. **43**, 142 (1989).

[30] Y. Mishima, M. Takei, T. Uematsu, N. Matsumoto, T. Kakehi, U. Wakino, and M. Okabe, J. Appl. Phys. **78**, 217 (1995).

[31] J. Narayan and C. W. White, Appl. Phys. Lett. **44**, 35 (1984).

[32] Y. Morita and T. Noguchi, Jpn. J. Appl. Phys. **28**, L309 (1989).

[33] S. M. Sze, Physics of Semiconductor Devices (Wiley, New York, 1981).

[34] D. E. Aspnes, A. A. Studna, and E. Kinsbron, Phys. Rev. B **29**, 768 (1984).

[35] S. Boultadakis, S. Logothetidis, and S. Ves, J. Appl. Phys. **72**, 3648 (1992).

[36] B. D. Cullity, Elements of X-ray Diffraction (Addison-Wesley, Reading, MA., 1967), Chap. 9, p. 264.

[37] S. Ghosh, A. Dasgupta, and S. Ray, J. Appl. Phys. **78**, 3200 (1995).

[38] Eva C. Freeman and W. Paul, Phys. Rev. B **20**, 716 (1979).

[39] A.-M. Dutron, E. Blanquet, N. Bourhila, R. Madar, and C. Bernard, Thin Solid Films **25**, 259 (1995).